Available online at www.sciencedirect.com

ScienceDirect

Geochimica et Cosmochimica Acta 185 (2016) 232–250

Geochimica et Cosmochimica Acta

www.elsevier.com/locate/gca

Magma transport and olivine crystallization depths in Kīlauea's east rift zone inferred from experimentally rehomogenized melt inclusions

Robin M. Tuohy [a,*], Paul J. Wallace [a], Matthew W. Loewen [a,b], Donald A. Swanson [c], Adam J.R. Kent [b]

[a] Dept. of Geological Sciences, University of Oregon, Eugene, OR 97403-1272, USA
[b] College of Earth, Ocean and Atmospheric Sciences, Oregon State University, Corvallis, OR 97331, USA
[c] Hawaiian Volcano Observatory, U.S. Geological Survey, Hawai'i National Park, HI 96718, USA

Received 1 September 2015; accepted in revised form 11 April 2016; available online 18 April 2016

Abstract

Concentrations of H_2O and CO_2 in olivine-hosted melt inclusions can be used to estimate crystallization depths for the olivine host. However, the original dissolved CO_2 concentration of melt inclusions at the time of trapping can be difficult to measure directly because in many cases substantial CO_2 is transferred to shrinkage bubbles that form during post-entrapment cooling and crystallization. To investigate this problem, we heated olivine from the 1959 Kīlauea Iki and 1960 Kapoho (Hawai'i) eruptions in a 1-atm furnace to temperatures above the melt inclusion trapping temperature to redissolve the CO_2 in shrinkage bubbles. The measured CO_2 concentrations of the experimentally rehomogenized inclusions ($\leqslant$590 ppm for Kīlauea Iki [$n = 10$]; $\leqslant$880 ppm for Kapoho, with one inclusion at 1863 ppm [$n = 38$]) overlap with values for naturally quenched inclusions from the same samples, but experimentally rehomogenized inclusions have higher within-sample median CO_2 values than naturally quenched inclusions, indicating at least partial dissolution of CO_2 from the vapor bubble during heating. Comparison of our data with predictions from modeling of vapor bubble formation and published Raman data on the density of CO_2 in the vapor bubbles suggests that 55–85% of the dissolved CO_2 in the melt inclusions at the time of trapping was lost to post-entrapment shrinkage bubbles. Our results combined with the Raman data demonstrate that olivine from the early part of the Kīlauea Iki eruption crystallized at <6 km depth, with the majority of olivine in the 1–3 km depth range. These depths are consistent with the interpretation that the Kīlauea Iki magma was supplied from Kīlauea's summit magma reservoir (~2–5 km depth). In contrast, olivine from Kapoho, which was the rift zone extension of the Kīlauea Iki eruption, crystallized over a much wider range of depths (~1–16 km). The wider depth range requires magma transport during the Kapoho eruption from deep beneath the summit region and/or from deep beneath Kīlauea's east rift zone. The deeply derived olivine crystals and their host magma mixed with stored, more evolved magma in the rift zone, and the mixture was later erupted at Kapoho.

Keywords: Volcanology; Melt inclusions; Geochemistry; Kīlauea; Hawaiian geology

1. INTRODUCTION

Melt inclusions provide a window into magmatic systems at depth by providing information on melt compositions, including volatiles, at the time of trapping. Melt inclusion studies at Hawaiian volcanoes have been used

* Corresponding author.
E-mail address: rmtuohy2@alumni.colostate.edu (R.M. Tuohy).

http://dx.doi.org/10.1016/j.gca.2016.04.020
0016-7037/

to investigate a variety of problems, from shallow magmatic processes during individual eruptions (Anderson and Brown, 1993; Wallace and Anderson, 1998; Edmonds et al., 2013; Thornber et al., 2015) to studies of mantle plume geochemistry and mantle heterogeneities (Hauri, 2002; Sobolev et al., 2011). These studies have improved our understanding of the eruption of high lava fountains (Sides et al., 2014a,b) and the details of Kīlauea's magma plumbing system (Edmonds et al., 2013, 2015; Rowe et al., 2015). At other oceanic islands such as La Réunion, olivine-hosted melt inclusions have also been used to constrain the size and shape of the magma plumbing system (Bureau et al., 1998a,b) and to understand individual eruptions (Vigouroux et al., 2009).

Melt inclusions that are rapidly quenched and naturally glassy are ideal for studying volatile concentrations (e.g., Johnson et al., 1994; Lloyd et al., 2013). In particular, the CO_2 and H_2O concentrations in melt inclusions can be used to infer olivine crystallization pressures and thus provide a tool for estimating magma storage depths (Anderson and Brown, 1993; Roggensack et al., 1997; Newman et al., 2000). However, determining the total volatile content of melt inclusions is complicated by the formation of shrinkage bubbles during post-entrapment cooling and crystallization (Anderson and Brown, 1993; Esposito et al., 2011; Steele-MacInnis et al., 2011; Hartley et al., 2014; Mironov et al., 2015; Moore et al., 2015; Wallace et al., 2015). Low solubility volatiles, like CO_2, partition strongly into these bubbles, depleting their concentration in the melt. As a result, the CO_2 measured in the glass by Fourier Transform Infrared Spectrometry (FTIR) or ion microprobe (SIMS) can greatly underestimate the amount of CO_2 that was present at the time of trapping (Esposito et al., 2011; Steele-MacInnis et al., 2011; Hartley et al., 2014; Mironov et al., 2015; Moore et al., 2015; Wallace et al., 2015).

A shrinkage bubble is formed during post-entrapment cooling and crystallization because of the negative volume change caused by crystallization of olivine along the inclusion-host interface and the fact that the melt in the inclusion contracts more than its crystalline host (Anderson, 1974; Roedder, 1979). This shrinkage causes a drop in pressure in the inclusion that leads to nucleation and growth of a vapor bubble (e.g., Lowenstern, 1995). During eruption, the shrinkage bubble will continue to expand with continued cooling, as the melt continues to contract more than the olivine host (Roedder, 1979; Anderson and Brown, 1993; Riker, 2005). Experimental heating of melt inclusions can redissolve the shrinkage bubble, returning some or all of the CO_2 to the glass (Wallace et al., 2015; Mironov et al., 2015). The main goal of our study was to investigate the use of a 1-atm furnace for heating of melt inclusions to redissolve CO_2 from bubbles. Our experimental results can be compared with other methods (micro-Raman and computational approaches) for assessing the extent of CO_2 loss to bubbles The second goal was to use the restored CO_2 contents of melt inclusions to calculate the pressures at which the inclusions were trapped in the olivine, thus providing information on crystallization depths beneath Kīlauea Volcano. Olivine crystallization depths can be used to constrain the depths of magma storage and transport, enabling a way to test magma plumbing models based on geophysical data.

1.1. Background on Kīlauea volcano and eruptions studied

1.1.1. Kīlauea's magma plumbing system

Kīlauea's magma plumbing system has been studied using geophysical (e.g. Eaton and Murata, 1960; Ryan et al., 1981; Poland et al., 2014) and geochemical (e.g. Wright and Fiske, 1971; Wright, 1973; Pietruszka and Garcia, 1999; Garcia et al., 2003; Thornber et al., 2003; Pietruszka et al., 2015) approaches to define the size, shape, and location of the summit magma body(s) and the interconnectedness between the summit and shallow rift zones (Eaton and Murata, 1960; Tilling and Dvorak, 1993). Most magma beneath the summit is currently stored in two reservoirs, one ca. 1–2 km deep near Halema'uma'u Crater and the larger ca. 2–5 km deep in the south caldera (Ryan et al., 1981; Ryan, 1988; Poland et al., 2014). These reservoirs have likely coexisted since at least the mid twentieth century (Wright and Klein, 2014; Pietruszka et al., 2015). Magma from summit storage is injected into the east rift zone 2–4 km below the surface (Poland et al., 2014), where it may be stored or later erupted (Wright and Fiske, 1971). Seismic data suggests that the rift zones are not likely deeper than 4–5 km, but the east rift zone has been proposed to extend to a depth of 6–9 km (Ryan, 1987; Delaney et al., 1990; Cayol et al., 2000; Wright and Klein, 2014).

Alternative rift zone models have been proposed in which dike injection occurs directly into the shallow rift zone from the mantle (Garcia et al., 2000) or from the décollement that marks the boundary between the volcanic pile and ocean floor (Clague and Denlinger, 1994; Vinet and Higgins, 2010). These alternatives are based in part on the primitive character of some lava erupted on the submarine lower east rift zone (Clague et al., 1995). At present, observations from the long-lived Pu'u 'Ō'ō eruption confirm the link between the summit and shallow rift zone, because rift zone tilt and inflation-deflation cycles closely follow those of the summit magma reservoir (Poland et al., 2014). Delaney et al. (1990) suggest that the summit and rift zone may be underlain by a thick, near vertical, dike-like magma system at a depth of 3–9 km, and Clague et al. (1995) proposed that the shallow and deep portions of the rift zone are interconnected by a series of bladed dikes that allow olivine to settle and accumulate across a large range of depths to form dunitic cumulate bodies.

1.1.2. Kīlauea Iki and Kapoho

The 1959 Kīlauea Iki eruption was unusual in many regards. It erupted outside the topographic summit caldera (see Supplementary Material, Figs. A.1 and A.3), produced the highest lava fountains ever recorded (ca. 600 m) at Kīlauea (Richter et al., 1970), contained abundant olivine (up to 20 wt.%) and MgO-rich glasses (up to 10 wt.%, indicating high eruptive temperatures up to 1192 °C; Murata and Richter, 1966; Wright, 1973; Helz, 1987; Pietruszka et al., 2015), and carried several different populations of olivine (deformed, megacrystic, reversely

zoned, sulfide-inclusion-bearing; Helz, 1987). Kīlauea Iki erupted two distinct magma types, widely referred to as S-1 (hot, volatile-rich) and S-2 (cool, stored) (Murata and Richter, 1966; Wright, 1973). The geochemical nature of the S-1 magma was considered to be unique, particularly its high CaO and Al_2O_3 (Wright, 1973; Helz, 1987; Wright and Klein, 2014), but these and other compositional attributes are now recognized as characteristics of summit lavas erupted from 1929 to 1959 (Pietruszka and Garcia, 1999; Garcia et al., 2003; Pietruszka et al., 2015). Earlier interpretations of the magma plumbing system suggested that volatile-rich S-1 magma triggered the eruption by bypassing the main summit reservoir to the NE, where it intercepted stored S-2 magma (Wright, 1973; Helz, 1987; Wright and Klein, 2006). However, recent studies suggest that rather than bypassing the summit reservoir, newly intruding magma filled and overflowed the reservoir (Wright and Klein, 2014; Pietruszka et al., 2015). Mixing of multiple magma components occurred during this process, and the resulting magma moved along the Halemaʻu maʻu-Kīlauea Iki Trend (Poland et al., 2014) to Kīlauea Iki Crater, where the eruption began (Wright and Klein, 2014; Pietruszka et al., 2015).

The 1960 eruption at Kapoho, ~47 km down the east rift zone from Kīlauea's summit (see Supplementary Material, Figs. A.1, A.3), is the rift extension of the 1959 Kīlauea Iki eruption (Richter et al., 1970). When the Kīlauea Iki eruption ended, the summit was more inflated than it had been before the eruption, and the outbreak at Kapoho occurred less than a month later (Richter et al., 1970). Similar to the Kīlauea Iki eruption, high lava fountains at Kapoho (up to 425 m) erupted very olivine-rich lava. A complex mixture of stored magmas and crystals was erupted at Kapoho (Wright and Helz, 1996). Early Kapoho lava was differentiated, interpreted as stored magma expelled from the rift zone (Richter et al., 1970; Wright and Fiske, 1971; Wright and Helz, 1996). Over the course of the Kapoho eruption, the eruptive temperature increased over a period of 10 days, and the lava became more MgO rich, with more abundant olivine, and less plagioclase and augite (Wright and Fiske, 1971). Kīlauea Iki's hotter, S-1 component erupted late in the eruption at Kapoho and was one of four magma components identified at Kapoho (Wright and Helz, 1996; Wright and Klein, 2014). The presence of the S-1 component likely produced the high lava fountains (Sides et al., 2014b) and the olivine-rich nature of the lava (Wright and Klein, 2014).

2. SAMPLE DESCRIPTIONS

Sampling focused in two regions: Kīlauea Iki Crater and near Pu'u Laimana in Kapoho, on Kīlauea's lower East Rift Zone (Fig. A.1). Full sample descriptions and location maps are given in the Supplementary Materials. Kīlauea Iki tephra samples were collected southwest of Kīlauea Iki crater off the Devastation Trail, near the base of a collapse pit that had previously been excavated by Bruce Houghton (University of Hawaii-Mānoa). These samples are exclusively from November 14–21 Episode 1 of the eruption, in contact with the much older Keanakākoʻi Tephra at the base of the collapse pit, and correspond with the IKI-2 and IKI-65 samples of Helz (1987) collected during the eruption. Kapoho sample numbers indicate the chronological order in which the samples were collected. Collection of 1960 Kapoho tephra was focused in a cinder quarry near Kapoho Cone (unrelated older cone, Fig. A.1), approximately 47 km away from Kīlauea's summit on the lower East Rift Zone. Stratigraphic relations of the tephra collected from Kapoho are shown in the Supplementary Appendix A, Fig. A.2. Eight samples were collected, focused on point sources for the eruption (Pu'u Laimana and Vent E) as well as the tephra plain and chaotic rafted terrain described by Hazlett (1993).

3. METHODS

3.1. Sample preparation

Tephra clasts were dried, gently crushed, and sieved at 1 phi intervals from 3 to >−1 phi (or 0.25 mm to 2+ mm) to separate olivine from its matrix glass. Following sieving, olivine crystals were selected from the 1 mm and larger size fractions under a binocular microscope. We prepared and analyzed naturally quenched melt inclusions from the Kīlauea Iki sample and from Kapaho samples Kap6 and Kap8. The purpose of analyzing these was to provide a reference data set for comparison with the melt inclusions that were experimentally rehomogenized to redissolve CO_2 from shrinkage bubbles.

3.2. Melt inclusion rehomogenization

Rehomogenization techniques were adapted from Rowe et al. (2006) and were used to redissolve vapor bubbles in melt inclusions from Kap4, Kap6, Kap8, and the Kīlauea Iki sample. For each experiment, approximately 20–40 olivine crystals were wrapped in a platinum foil 'taco' and suspended with platinum wire on aluminum rods within a 1-atm Deltec furnace. The platinum foil taco was held outside the furnace hot zone while the furnace was brought to temperature (800–1400 °C), and the oxygen fugacity was maintained at the fayalite-magnetite-quartz (FMQ) buffer with a hydrogen and CO_2 gas mixture. The target furnace temperature was initially chosen based on an estimate of the formation temperature of the olivine host using the Thornber et al. (2003) high-Fo olivine thermometer. Using published data for the Kapoho eruption (Wright and Helz, 1996), this temperature was calculated to be ~1240 °C. Several experiments were conducted at this temperature but appeared to be unsuccessful in dissolving shrinkage bubbles based on visual inspection of the reheated melt inclusions. Heating experiments on melt inclusions from a Mauna Loa picrite using a high temperature heating stage found that temperatures as high at 1420 °C were necessary to redissolve shrinkage bubbles (Wallace et al., 2015), so we chose 1400 °C as our experimental temperature. Such high temperatures (overheating above original magmatic trapping temperature) is necessary because we conducted the rehomogenization experiments at 1-atm pressure rather than at a higher pressure appropriate for the original

trapping conditions (Schiavi et al., 2016). Some experiments were conducted at 1300 °C in order to assess the effect of temperature on rehomogenization and potential loss of H by diffusion through the olivine host.

In our experiments, when the furnace was at the desired temperature, the olivine crystals were lowered into the furnace hot zone. The crystals were held at temperature for no more than 15 min. Running electrical current through the wire cut the platinum wire, and the samples were drop-quenched into a cool, water-filled bulb at the base of the furnace. The olivines were then removed from the platinum foil, and crystals or crystal fragments with melt inclusions were selected for analysis. Many of the olivine crystals in each of the experiments broke into numerous smaller fragments, either during heating or during the drop quench. Because of this and the large number of crystals in each experiment (~20–40), we did not do a before and after examination of individual melt inclusions.

Some melt inclusions developed cracks in the host olivine during preparation for FTIR analysis (Fig. 1). Melt inclusions with cracks visible prior to preparation were not selected for analysis. Any melt inclusions that had cracks in the olivine host before the heating experiment would have lost all volatiles (Nielsen et al., 1998), and this did not occur for any of the melt inclusions analyzed in this study.

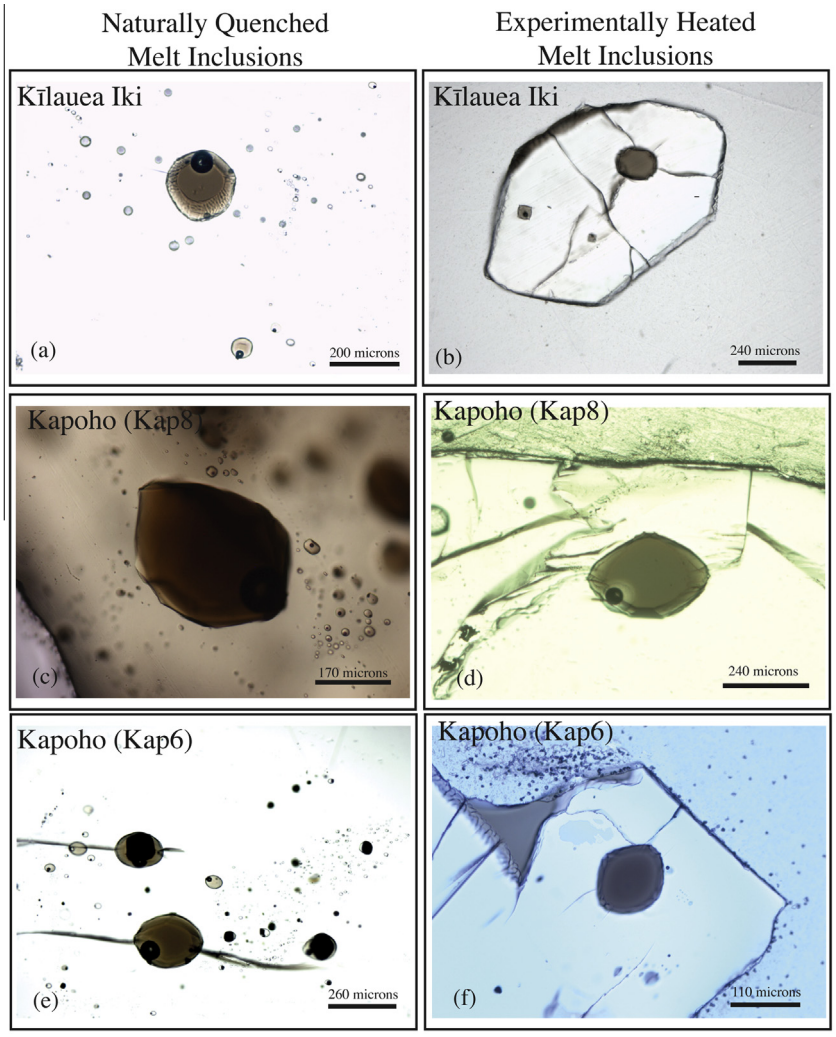

Fig. 1. Photo mosaic of naturally quenched and experimentally heated melt inclusions analyzed in this study. Naturally quenched melt inclusions have a variety of textures, and experimental heating results in some modification of these (Note: These are not photos of individual inclusions before and after heating). Cracks in the olivine host may be observed in several images. These cracks developed during preparation of the olivine wafer for FTIR analysis. (a and b) Kīlauea Iki melt inclusions. The naturally quenched melt inclusion (a) has wavy walls (along the inclusion/host interface) and a large vapor bubble. Note that the 'ring' inside the inclusion is an artifact of sectioning. The heated melt inclusion (b) has an ellipsoidal shape and lacks a vapor bubble. (c and d) Kap8 melt inclusions. The naturally quenched melt inclusion (c) is dark brown, ellipsoidal in shape, and contains a large shrinkage bubble in the lower right corner of the inclusion. The heated melt inclusion (d) has a halo around its vapor bubble, which may indicate that the bubble did not completely dissolve, or that the CO_2 did not have enough time to diffuse into the glass. (e and f) Kap6 melt inclusions. The naturally quenched melt inclusion (e) is pictured with other melt inclusions in which a Cr-spinel accessory phase was co-trapped with silicate melt. The heated melt inclusion (f) contains no bubble and has wavy walls.

Table 1
Melt inclusion volatile contents, vapor saturation pressures, and olivine crystallization depths.

Sample	Melt inclusion	H_2O (wt.%)	CO_2 (ppm)	Corr. factor	H_2O cor.	CO_2 cor.	H_2O (% SE)	CO_2 (% SE)	Host Fo	Diam. (μm)	Psat (bars)	Depth (km)
Kīlauea Iki	Kil-Iki_Nat-1	0.41	b.d.	0.90	0.37	b.d.	9	9	86.1	120	14	–
NQ	Kil-Iki_Nat-2	0.30	198	0.87*	0.26	172	12	13	–	90	380	–
	Kil-Iki_Nat-3	0.40	127	0.86	0.34	110	4	5	87.9	130	250	–
	Kil-Iki_Nat-4	0.49	b.d.	0.88*	0.43	b.d.	4	4	–	350	19	–
	Kil-Iki_Nat-6	0.74	b.d.	0.86	0.64	b.d.	1	10	87.0	200	37	–
	Kil-Iki_Nat-8	0.60	226	0.87*	0.52	197	10	10	87.9	193	452	–
	Kil-Iki-Nat-9	0.52	118	0.90	0.47	106	5	17	85.6	160	252	–
	Kil-Iki-Nat-10A	0.56	154	0.87	0.49	134	5	7	87.4	220	314	–
	Kil-Iki-Nat-10B	0.55	126	0.87*	0.48	110	5	6	87.4	350	262	–
	Kil-Iki-Nat-11A	0.54	102	0.87	0.47	88	3	20	86.5	210	214	–
	Kil-Iki-Nat-11B	0.64	158	0.90	0.58	142	3	3	86.5	160	341	–
	Kil-Iki-Nat-12	0.39	471	0.88*	0.34	415	3	14	–	150	914	–
	Kil-Iki-Nat-13	0.56	168	0.88*	0.49	148	3	9	85.0	175	343	–
	Kil-Iki-Nat-14A	0.38	131	0.85*	0.32	112	4	11	87.6	100	253	–
	Kil-Iki-Nat-14B	0.38	258	0.85	0.32	220	4	5	87.6	180	485	–
	Kil-Iki-Nat-15	0.48	62	0.86	0.41	53	8	11	87.1	120	133	–
	Kil-Iki-Nat-16	0.06	138	0.88*	0.05	122	12	25	–	130	265	–
	Median	0.49	146	0.87	0.43	112	4	10	87.0	160	262	
Kīlauea Iki	Kil-Iki-R-2	0.14	215	1.33	0.19	285	6	5	87.9	130	617	2.6
1400 °C	Kil-Iki-R-3	0.12	433	1.36*	0.17	588	4	7		230	1239	4.7
	Kil-Iki-R-6A	0.08	110	1.32*	0.11	145	8	8	87.5	120	316	1.4
	Kil-Iki-R-6B	0.07	105	1.32*	0.09	139	7	14	87.5	120	303	1.4
	Kil-Iki-R-8	0.08	108	1.32	0.11	142	3	4	87.7	100	309	1.4
	Kil-Iki-R-10	0.18	b.d.	1.36*	0.24	b.d.	5	32	–	110	6	0.1
	Kil-Iki-R-12	0.09	140	1.34*	0.12	187	0	7	–	230	407	1.8
	Kil-Iki-R-14	0.10	426	1.30	0.13	554	3	15	86.5	100	1168	4.5
	Kil-Iki-R-13	0.29	183	1.34*	0.38	246	2	4	–	175	544	2.3
	Kil-Iki-R-15	0.05	156	1.30*	0.07	202	4	4	–	130	438	1.9
	Median	0.10	156	1.32	0.13	195	4	7	87.5	125	423	1.8
Kap6	Kap6-Nat-1	1.19	97	0.85	1.01	82	7	8	86.8	248	277	–
NQ	Kap6-Nat-2	0.58	306	0.82	0.47	251	5	6	87.8	320	561	–
	Kap6-Nat-3	0.91	260	0.87	0.79	226	4	4	86.2	200	546	–
	Kap6-Nat-4	0.55	233	0.87	0.47	202	5	41	86.1	215	459	–
	Kap6-Nat-5	1.15	112	0.97	1.12	108	3	8	81.6	190	357	–
	Kap6-Nat-6	0.66	91	0.82	0.54	75	3	9	88.1	180	191	–
	Kap6-Nat-7	0.72	175	0.95	0.68	167	4	4	81.8	250	403	–
	Median	0.72	175	0.87	0.68	167	4	8	86.2	215	403	
Kap6	Kap6-R-1	0.25	158	1.16*	0.29	183	4	4	87.9	90	405	1.8
1400 °C	Kap6-R-2	0.14	318	1.08*	0.15	343	9	9	-	130	737	2.9
	Kap6-R-3	0.24	404	1.09	0.26	440	3	2	89.6	125	942	3.7
	Kap6-R-4	0.19	197	1.21	0.23	238	3	4	87.0	120	519	2.2
	Kap6-R-5	0.43	183	1.26	0.54	231	5	8	88.0	145	525	2.2
	Kap6-R-6	0.22	93	1.20	0.26	112	20	0	87.8	128	253	1.2
	Kap6-R-10	0.26	124	1.20*	0.31	148	2	3	–	135	331	1.5
	Kap6-R-11	0.11	93	1.17*	0.13	109	2	9	–	90	247	1.1
	Median	0.23	171	1.20	0.26	207	4	4	87.9	126	462	2.0
Kap8	K99-9-12	0.22	288	0.85*	0.19	245	18	20	–	135	532	–
NQ	K99-9-16	0.62	212	0.85	0.53	180	1	5	87.3	225	417	–
	K99-9-17	0.25	137	0.81	0.20	111	5	9	88.0	120	246	–
	Kap8-Nat-1	0.10	106	0.80*	0.08	85	11	24	–	140	185	–
	Kap8-Nat-2	0.49	152	0.80*	0.39	122	14	14	–	150	280	–
	Kap8-Nat-4	0.31	284	0.80*	0.25	227	2	6	–	–	496	–
	Kap8-Nat-8a	0.56	85	0.94	0.53	80	2	3	87.5	260	201	–
	Kap8-Nat-8b	0.62	76	0.95*	0.59	72	2	2	87.5	150	191	–
	Kap8-Nat-9	0.10	143	0.89	0.09	128	4	3	85.0	230	278	–
	Median	0.31	143	0.87	0.25	122	4	6	87.5	150	278	

Kap8	Kap8-12	0.19	392	1.15*	0.21	451	7	11	–	90	962	3.5
1400 °C	Kap8-13B	0.16	275	1.15*	0.18	317	6	17	–	120	683	2.7
	Kap8-15	0.29	1566	1.19	0.35	1863	1	0	89.7	163	3542	12.1
	Kap8-20	0.15	103	1.29	0.19	132	19	21	88.2	200	291	1.3
	Kap8-18	0.21	190	1.31	0.28	253	5	9	87.9	130	552	2.3
	Kap8-22	0.15	387	1.23*	0.19	475	18	4	–	110	1012	3.9
	Kap8-23	0.15	167	1.27*	0.19	212	2	3	–	150	462	2.0
	Kap8-25	0.16	532	1.15*	0.19	612	25	6	–	120	1288	4.9
	Kap8-28	0.16	719	1.23*	0.20	884	4	5	–	150	1818	6.6
	Kap8-31	0.06	377	1.23*	0.07	463	6	5	–	70	984	3.8
	Kap8-32	0.16	494	1.17	0.19	578	4	6	89.4	190	1219	4.6
	Kap8-34	0.10	257	1.23*	0.12	316	7	7	–	110	679	2.7
	Kap8-35	0.08	433	1.15*	0.09	498	4	4	–	100	1054	4.1
	Kap8-39	0.06	471	1.15*	0.07	542	8	11	–	100	1143	4.4
	Kap8-40	0.06	274	1.23*	0.07	337	12	13	–	90	723	2.9
	Kap8-41	0.10	421	1.23*	0.12	518	5	6	–	80	1096	4.2
	Kap8-R-50	0.23	364	1.17	0.27	425	6	2	89.5	185	912	3.6
	Kap8-R-51	0.08	334	1.25	0.10	418	3	3	87.8	90	890	2.6
	Kap8-R-52	0.16	302	1.22	0.20	368	2	3	88.6	155	790	3.2
	Kap8-R-54	0.25	77	1.23*	0.31	93	2	4	–	137	213	1.0
	Kap8-R-55	0.16	437	1.02	0.16	446	2	3	88.2	109	950	3.7
	Median	0.16	377	1.21	0.19	446	5	5	88.2	120	950	3.6
Kap4	Kap4-R-3	0.12	344	1.25*	0.14	429	3	4	–	90	916	3.6
1400 °C	Kap4-R-4	0.19	410	1.14*	0.22	468	4	11	–	110	997	3.9
	Kap4-R-7	0.17	569	1.25*	0.22	712	3	10	–	100	1486	5.6
	Kap4-R-8	0.08	102	1.14*	0.09	116	17	19	–	90	253	1.2
	Kap4-R-9	0.18	407	1.16	0.21	472	4	7	89.1	130	1006	3.9
	Kap4-R-10	0.46	410	1.26	0.58	517	2	4	87.7	220	1122	4.3
	Kap4-R-12	0.14	561	1.25	0.18	701	10	12	85.2	140	1464	5.5
	Kap4-R-6	0.09	297	1.26*	0.15	374	3	5	–	100	801	3.2
	Kap4-R-14	0.21	208	1.12	0.24	233	2	8	88.3	100	508	2.1
	Median	0.17	407	1.21	0.21	468	3	8	88.0	100	997	3.9
Kap8	Kap8-1300-2	0.31	22	1.04	0.32	22	5	22	87.8	233	60	0.4
1300 °C	Kap8-1300-3	0.15	38	1.04	0.16	40	5	5	87.6	213	90	0.4
	Kap8-1300-4	0.26	117	1.12	0.29	131	17	6	85.4	118	294	1.3
	Kap8-1300-5	0.74	287	1.12	0.83	322	1	20	85.2	294	753	3.1
	Kap8-1300-6	0.69	275	1.11	0.76	306	1	0	85.5	213	708	3.0
	Kap8-1300-7	0.24	74	1.03	0.25	77	5	7	88.2	161	173	0.9
	Kap8-1300-8	0.45	116	1.04	0.47	121	4	27	87.6	188	285	1.3
	Kap8-1300-9	0.46	177	1.02	0.47	180	2	2	87.7	192	411	1.8
	Kap8-1300-10	0.39	248	1.12	0.44	278	3	4	85.3	127	617	2.6
	Median	0.39	117	1.04	0.44	131	4	6	87.6	192	294	1.3

Sample numbers. NQ indicates naturally quenched inclusions. Temperatures of rehomogenization are indicated for heated inclusions.
Melt inclusion (MI) identifiers. MIs with "Nat" indicate a naturally quenched inclusion. MIs with an "R" indicate an experimentally heated MI. MIs with a letter following their sample number indicate that multiple inclusions were analyzed within a single olivine host.
Uncorrected H_2O measurements by FTIR using the OH-absorbance peak at 3550 cm^{-1}.
Uncorrected CO_2 measurements by FTIR using the carbonate doublet at 1430 and 1515 cm^{-1}.
Correction Factors: NQ inclusions were corrected for post-entrapment crystallization using Petrolog3.1. Heated inclusions were corrected for the effect of olivine dissolution during the experiment using Petrolog3.1. The correction factor is based on the Petrolog results and shows how much an incompatible element is affected by PEC or olivine dissolution. Values >1 indicate olivine dissolution during heating, and the analyzed values of H_2O and CO_2 must be multiplied by the correction factor to get their concentrations in the melt inclusion at the original time of trapping. Values <1 are typical for naturally quenched inclusions.
H_2O and CO_2 standard error (SE) values: Uncertainties were calculated using Gaussian error propagation based on replicate absorbance and thickness measurements.
Average diameter of melt inclusions was determined assuming an ellipsoidal shape.
Vapor saturation pressures were calculated using the solubility model of Newman and Lowenstern (2002) at 1200 °C and SiO_2 of 49 wt.%.
Estimated depths of olivine crystallization: We used the depth-density relationship of Ryan (1987) in which density in the shallow crust at Kilauea is lower due to the presence of vapor-filled cracks, and the crustal density increases with depth and approaches the density of unfractured basalt at >4 km depth.
Depths are not reported for naturally quenched inclusions because loss of CO_2 to shrinkage bubbles renders calculated depths inaccurate.
* MIs for which H_2O and CO_2 were measured but not major element composition. These inclusions were corrected using the correction factor of another inclusion with similar host composition from the same sample or, if the host olivine was not analyzed, using the average correction factor for other inclusions from the same sample.

3.3. Melt inclusion glass analysis

The H_2O and CO_2 contents of melt inclusions were determined by Fourier Transform Infrared (FTIR) spectroscopy using a Thermo-Nicolet Nexus 670 FTIR spectrometer interfaced with a Continuum IR microscope at the University of Oregon. A full description of analytical procedures is given in the Supplementary Materials. The H_2O and CO_2 data are reported in Table 1. Based on combined uncertainties in measured wafer thicknesses (±5%, one standard error) and IR absorbance values, the average uncertainty (one standard error) for naturally quenched melt inclusions is ±0.02 wt.% for H_2O and ±13 ppm for CO_2, and for heated inclusions, ±0.02 wt.% for H_2O and ±25 ppm for CO_2.

Melt inclusion wafers were mounted in epoxy and analyzed for major elements by electron microprobe (Cameca SX-100) at the University of Oregon. The major elements Si, Mg, Al, Fe, Ca, Na, K, and Mn were analyzed with a 10 nA sample current, 10 micron diameter beam, and 15 kV accelerating voltage. A higher current (50 nA) was used to increase sensitivity for Ti, S, Cl, P, and F. Time-dependent intensity corrections were used for Si, Al, Na, and K to correct for the effects of alkali migration in the glass, though the effects of migration were quite minor. Melt inclusions were typically analyzed in three spots. Olivine hosts were analyzed for major elements (Mg, Fe, Al, Mn, Si) using a 30 nA sample current, 10 micron diameter beam, and 15 kV accelerating voltage. Three spots on the host were analyzed within a few 100 microns of the inclusion(s) of interest. Tephra groundmass glass was analyzed from Kapoho samples Kap8 and Kap6. The operating conditions for the tephra glass used a 30 nA beam current for all elements because the degassed nature of the glass resulted in negligible alkali migration (based on time-dependent intensity variations) during analysis and because we did not need to measure S, Cl, and F. Analysis of a secondary standard of H_2O-poor basaltic glass showed that both analytical conditions yielded similar results for the major elements. The major element data for melt inclusions, host olivine, tephra groundmass glass, and the secondary standard are reported in Supplementary Table 1.

Trace element analyses of the melt inclusions were carried out by laser ablation-inductively coupled plasma-mass spectrometry (LA-ICP-MS) at Oregon State University using a Photon Machines G2 193 nm Ar-F laser attached to a Thermoscientific Xseries2 quadrupole mass spectrometer with instrument conditions and data processing similar to that in Loewen and Kent (2012). Melt inclusions were analyzed using a 50 μm spot at 7 Hz for approximately 30 s. GSE-1G was used as a calibration standard, whereas GSD-1G and natural glasses (BHVO-2G, BCR-2G) were used as secondary standards. Data were processed using in-house LaserTRAM and LaserCalc software, which use a Visual Basic script operated in Microsoft Excel. These programs allow for manual selection of a 20–30 s background interval and a 15–30 s ablation interval. The software normalizes each analyte mass to the ^{43}Ca internal standard and calculates a concentration of the analyte using the Ca concentrations determined by electron microprobe. All trace element data are reported in Supplementary Table 1.

4. RESULTS

4.1. Melt inclusion textures

The naturally quenched melt inclusions are spherical to ellipsoidal in shape, medium to dark brown in color, and typically contain one vapor bubble and less commonly an accessory phase like Cr-spinel or magnetite (Fig. 1). It is possible that some larger bubbles were entrapped with melt, but most bubbles are likely post-entrapment in origin (Moore et al., 2015). Some melt inclusions did not contain bubbles, but bubble-free inclusions were similar to bubble-bearing inclusions in major element and host olivine compositions. Some naturally glassy inclusions from Kīlauea Iki have a wavy, irregularly textured interface between the melt inclusion and the host (Fig. 1a), and this texture is much more common in heated melt inclusions (Fig. 1d, f). Heated melt inclusions retained their spherical to ellipsoidal shape, but some no longer contained a shrinkage bubble (Fig. 1b, f) or had a relatively small bubble compared to the naturally quenched inclusions (bubble diameters in inclusions heated to 1400 °C were ~50% smaller than those in naturally quenched inclusions). Wallace et al. (2015) noted that in some cases, experimentally rehomogenized Mauna Loa melt inclusions nucleated a small bubble on quenching, even though the vapor bubble had totally redissolved during the experiment.

4.2. Melt inclusion and olivine compositions

The first step in interpreting the analytical data was to assess whether the composition of the glass in each inclusion was in equilibrium with its olivine host (Fig. 2). The naturally quenched melt inclusions plot below the olivine-melt equilibrium line because of post-entrapment crystallization, which causes melt inclusions to have an Mg/Fe ratio that is too low to be in equilibrium with the olivine host (e.g., Danyushevsky et al., 2002a). In contrast, the heated melt inclusions plot above the equilibrium line (Fig. 2), indicating they have Mg/Fe ratios that are too high to be in equilibrium with the olivine host. This is likely the result of heating above the original trapping temperature, which causes excess olivine dissolution from the inclusion walls (Danyushevsky et al., 2000; Wallace et al., 2015). Increasing distance above the equilibrium line (Fig. 2) indicates greater amounts of olivine dissolution during heating. Melt inclusions that were heated to 1300 °C lie closer to the melt-olivine equilibrium line than those heated to 1400 °C.

Correction of melt inclusion compositions for the effects of post-entrapment crystallization (PEC) must take into account the effects of Fe-diffusive loss (Danyushevsky et al., 2002b). Most of the naturally quenched melt inclusions from Kīlauea Iki (Fig. 3a) and Kapoho (Fig. 3b) have lost some Fe by diffusion, as most fall below the trend line for the bulk rock (Richter et al., 1970) and matrix glass data. The Kīlauea Iki and Kapoho heated melt inclusions can be grouped into three categories: (1) melt inclusions

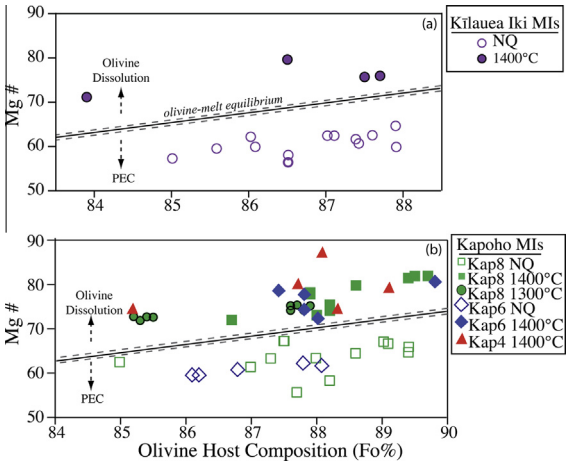

Fig. 2. Mg# (=100 Mg/[Mg + Fe^{2+}]) of naturally quenched (NQ) and heated melt inclusions vs. the host olivine composition. The olivine-melt equilibrium line is for a K_d value of 0.33 ± 0.01, as calculated by Petrolog3.1. Increasing distance below the olivine-melt equilibrium line indicates increasing amounts of post-entrapment crystallization. Increasing distance above the olivine-melt equilibrium line indicates increasing amounts of olivine dissolution caused by overheating during the experiment.

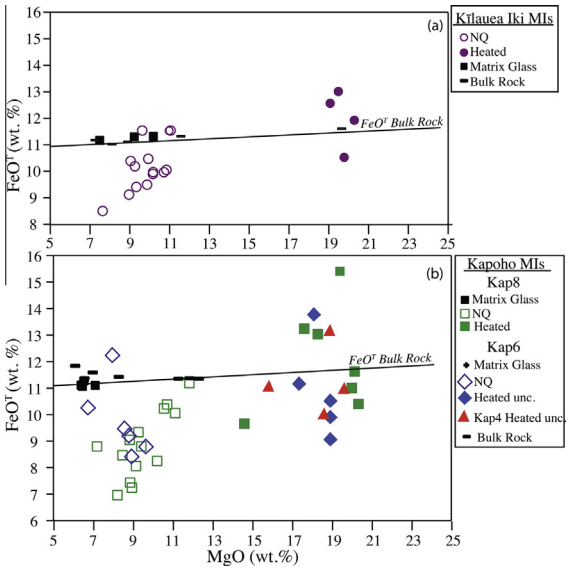

Fig. 3. MgO (wt.%) vs. FeO^T (wt.%) for melt inclusions and matrix glass from (a) Kīlauea Iki and (b) Kapoho. Also shown is the average bulk rock and matrix glass compositions from Kīlauea Iki sample Iki-22 (a) and the average bulk rock composition from Kapoho (F1, F5, F7, F8, F14, F16, and F20) (b) (Richter et al., 1970). Matrix glass analyses for Kap6 and Kap8 are from this study (Supplementary Table 1). A best fit line is drawn through the bulk rock and matrix glass data for each eruption. Note that the matrix glass data for Kap6 is virtually identical to that for Kap8, and as a result, the symbols (small black diamonds) are obscured on the figure. Raw (uncorrected) melt inclusion compositions are plotted for naturally quenched, 1300 °C, and 1400 °C heated melt inclusions. Most naturally quenched (NQ) melt inclusions from all suites fall below this line, suggesting that the melt inclusions lost Fe by diffusion during post-entrapment crystallization. These melt inclusions can be corrected by selecting an appropriate FeO^T value from the best fit line for a given MgO content of the melt inclusion. Heated melt inclusions plot to the right of the natural inclusions because they have greater amounts of MgO from olivine dissolution during overheating. Heated melt inclusions that plot below the line likely did not regain all of the Fe lost by diffusion. Heated inclusions that plot above the best fit line may have been affected by dissolution of an Fe-rich accessory phase during reheating (e.g., Rowe et al., 2006).

plotting below the line lost Fe either naturally or during the heating process; (2) melt inclusions plotting on the trend line either did not lose Fe or were able to recover their lost Fe from the zone of olivine immediately adjacent to the inclusion-host interface that remelted during the experiment; and (3) melt inclusions plotting above the trend line may have contained a co-entrapped Cr-spinel crystal that was partially or completely dissolved during reheating (Rowe et al., 2006).

The PEC correction involves incrementally adding olivine back into the melt composition until it is in equilibrium with its host. All PEC and Fe-loss corrections were done using Petrolog3.1 (Danyushevsky and Plechov, 2011). We assumed an oxidation state at the FMQ buffer ($FeO/FeO^T = 0.85$; Rhodes and Vollinger, 2005), and the calculated K_d value of 0.33 ± 0.01 is consistent, within uncertainty, with the K_d value of 0.340 ± 0.012 determined by Matzen et al. (2011) for Hawaiian tholeiitic melts. The data for H_2O and CO_2 were corrected by assuming incompatible behavior during PEC. Some melt inclusions were analyzed for H_2O and CO_2 but not for major elements, and for those, we used the PEC value of other inclusions with similar host composition from the same sample or the average PEC of other inclusions from the same sample to correct the H_2O and CO_2 values (Table 1). The target FeO^T value of 11.2–11.3 wt.% for the Kīlauea eruptions studied was selected based on whole rock (Richter et al., 1970) and matrix glass data. We investigated how much the choice of FeO^T values affects the Petrolog corrections, because it is well documented that Kīlauea tholeiitic magmas can have a range in FeO^T (e.g., Clague et al., 1995; Garcia et al., 2003). Using values of FeO^T from 10.8–11.4 wt.% (appropriate for lavas with >8 wt.% MgO) primarily affects the restored MgO contents of the inclusions but has a negligible effect on the other major element and volatile concentrations. The corrected melt inclusion compositions are given in Supplementary Table 1.

The average amount of post-entrapment crystallization for the naturally quenched inclusions, including the effects of Fe loss, is 14 ± 3.6% for Kīlauea Iki ($n = 13$) and 13 ± 8.3% for Kapoho ($n = 20$). In the few cases where we analyzed multiple inclusions in the same host crystal ($n = 4$), we found similar extents of PEC. For heated melt inclusions, the Petrolog calculations incrementally removed olivine from the analyzed composition of the glass to correct for the effects of olivine dissolution during the experimental heating. The average calculated amount of olivine dissolution for Kīlauea Iki melt inclusions heated to 1400 °C ($n = 4$) is 25 ± 3.3. Kapoho melt inclusions heated to 1400 °C ($n = 17$) have an average of 17 ± 7% dissolution, and those heated to 1300 °C ($n = 9$) show less dissolution, with an average of 7 ± 3.6%.

4.3. Volatiles

4.3.1. Naturally quenched melt inclusions

Kīlauea Iki naturally quenched melt inclusions mostly have 0.26–0.64 wt.% H_2O (Table 1; Fig. 4a), but there is one inclusion with a very low value of 0.05 wt.%. Concentrations of CO_2 range from below the detection limit (~20–30 ppm) to 415 ppm (Table 1). For comparison, published melt inclusion data from Episode 1 of the Kīlauea Iki eruption (sample Iki-22) have values of 0.25–0.95 wt.% H_2O and below detection to 350 ppm CO_2 (Anderson and Brown, 1993) and 0.46–0.64 wt.% H_2O and below detection to 650 ppm CO_2 (Sides et al., 2014b). Naturally quenched melt inclusions from Kapoho have ~0.1 to 1.1 wt.% H_2O and <100 to 251 ppm CO_2. H_2O values higher than 0.7 wt.% are present in Kap8 inclusions only (Fig. 4b). For comparison, Sides et al. (2014b) found 0.41–0.54 wt.% H_2O and 25–283 ppm CO_2 in Kapoho melt inclusions. H_2O and CO_2 contents for our naturally quenched Kapoho inclusions overlap with values for Kīlauea Iki.

4.3.2. Heated melt inclusions

Heated melt inclusions from Kīlauea Iki range from 0.07 to 0.38 wt.% H_2O and below detection to 588 ppm CO_2 (Table 1; Fig. 4a). When heated melt inclusions are compared to naturally quenched inclusions from the same samples, many heated inclusions have values in the range of 0.1–0.2 wt.% H_2O, lower than all but one of the naturally quenched inclusions (Fig. 4a). Thus, it appears that hydrogen diffusive loss occurred during the experiments. Heated Kīlauea Iki melt inclusions have higher median CO_2 concentrations (195 ppm; we use median values for CO_2 because of non-normal distributions) than the naturally quenched ones (112 ppm), suggesting the reheated inclusions gained CO_2 from shrinkage bubbles during the experiments, but there is significant overlap between the two data sets (Figs. 4a and 5).

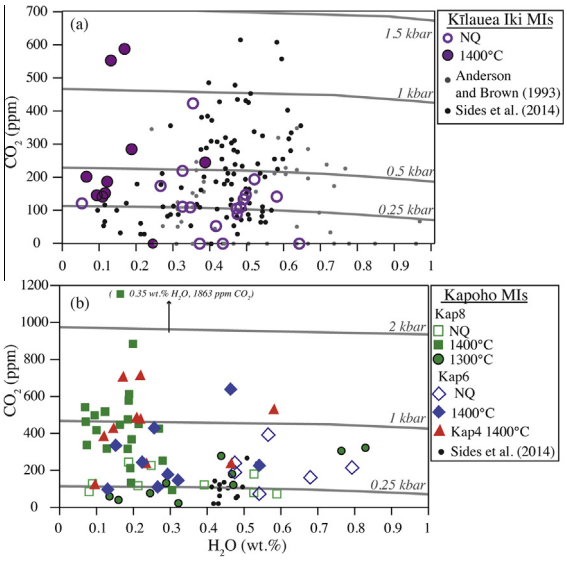

Fig. 4. Melt inclusion H_2O vs. CO_2 for naturally quenched and heated inclusions from Kīlauea Iki (a) and Kapoho (b). Kīlauea Iki melt inclusions from Anderson and Brown (1993) are shown by small filled gray circles. Kīlauea Iki (a) and Kapoho (b) melt inclusions from Sides et al., 2014a,b are shown as small black circles. Temperatures reported are for heated samples. Plots include corrected data only. Naturally quenched melt inclusions are shown as open symbols and heated melt inclusions as filled symbols. Vapor saturation isobars (calculated using Newman and Lowenstern [2002] are shown by gray curves. CO_2 values below detection limit (~20–30 ppm) are plotted along the x-axis. Note that one Kapoho inclusion plots off scale at 1863 ppm CO_2.

Kap8 melt inclusions that were heated to 1300 °C have a wide range of H_2O contents (Fig. 4b; Table 1). Fewer inclusion have low values (Fig. 4b), and therefore may not have experienced as much hydrogen diffusive loss during heating. However, the inclusions heated to 1300 °C have lower CO_2 (below detection to 322 ppm CO_2) than the inclusions heated to 1400 °C (Table 1). The inclusions heated to 1300 °C have H_2O and CO_2 values that overlap with most of the naturally quenched Kapoho melt inclusions (Fig. 4b). Kap8 melt inclusions heated to 1300 °C did dissolve olivine from the inclusion walls during heating (~15–20 wt.% olivine based on MgO contents of the glasses), but the similarity of CO_2 values in the 1300 °C and naturally quenched inclusions (Fig. 5) suggest the temperature was not high enough to redissolve CO_2 from vapor bubbles.

The Kapoho naturally quenched melt inclusions have ~0.1 to 1.1 wt.% H_2O and ~70–250 ppm CO_2 (Fig. 4b). Heated melt inclusions (1400 °C) have ~0.1 to 0.58 wt.% H_2O, which overlaps with naturally quenched inclusions but is mostly at the low end of the range. The lower values are suggestive of hydrogen diffusive loss. The heated (1400 °C) Kapoho melt inclusions have a wide range of CO_2 values, from 93 to 884 ppm CO_2, with one inclusion containing 1863 ppm CO_2 (Figs. 4b, 5). As with Kīlauea Iki, there is substantial overlap of CO_2 values in heated and naturally quenched inclusions. However, the heated inclusions include many higher values (Fig. 5) and have higher within-sample median concentrations than unheated inclusions (Table 1).

5. DISCUSSION

5.1. Hydrogen loss by diffusion

Heating olivine-hosted melt inclusions was successful in redissolving at least some of the CO_2 from shrinkage bubbles (Fig. 5). However, the high temperature that was necessary to redissolve CO_2 appears to have resulted in hydrogen diffusive loss from the melt inclusions based on their low H_2O contents ($\leqslant$0.2 wt.%) compared to the naturally quenched inclusions (Fig. 4). Also, there is a weak positive correlation ($R^2 = 0.4$) between H_2O content and inclusion size for heated Kapoho inclusions (Fig. 6a). Furthermore, some of the heated melt inclusions are relatively small compared to the size range of the naturally quenched melt inclusions (Fig. 6a), and the smaller size appears to show the most hydrogen diffusive loss, as expected given their larger surface/volume ratio (e.g., Qin et al., 1992; Lloyd et al., 2013). The size difference between the naturally

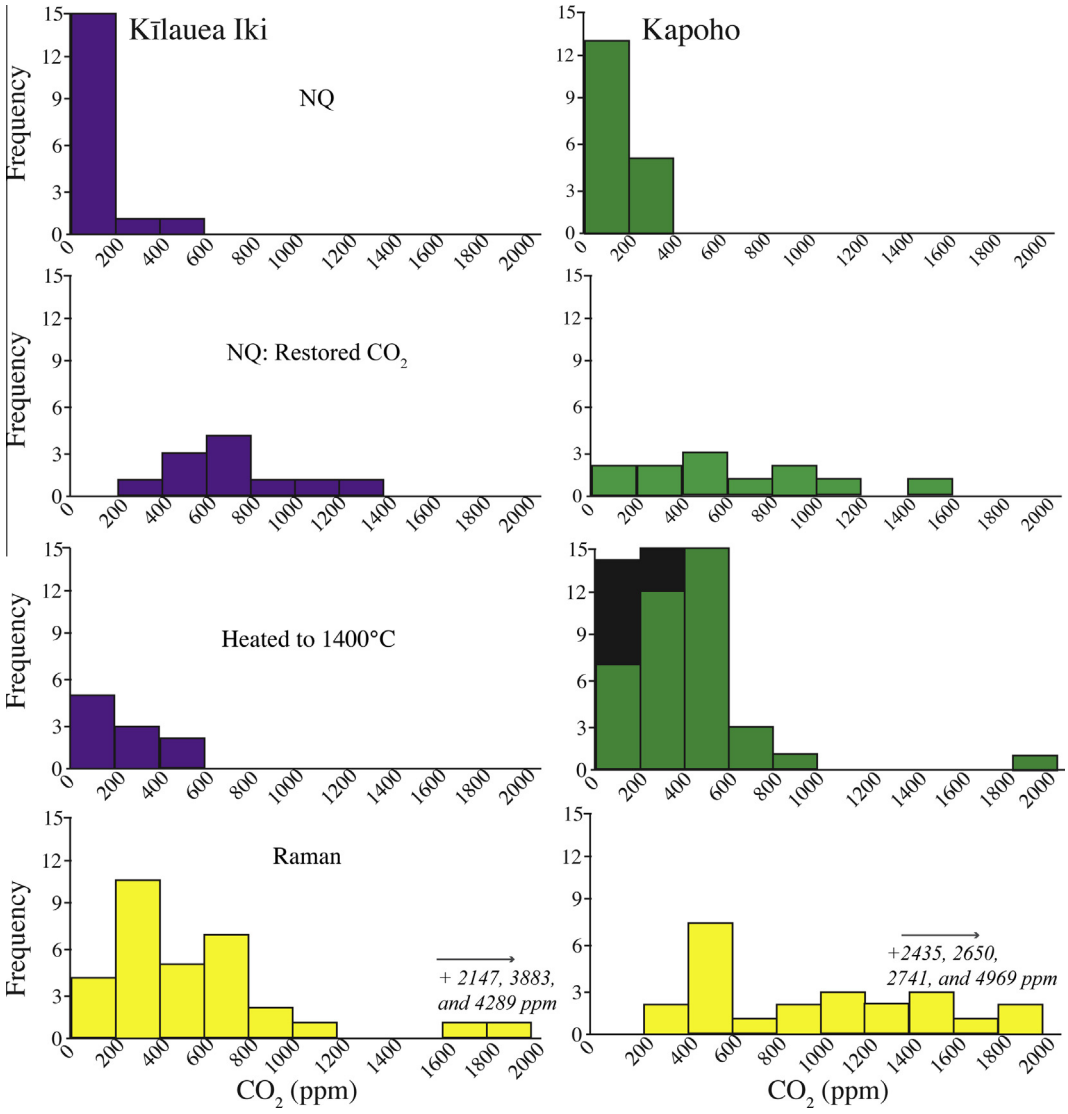

Fig. 5. Histograms showing the CO_2 concentrations measured in naturally quenched (NQ) melt inclusions (top panels) compared to CO_2 concentrations restored by various methods. The second row shows restored CO_2 concentrations for the naturally quenched inclusions using a cooling and crystallization model (Riker, 2005; Wallace et al., 2015). The third row shows the experimentally heated inclusions. For Kapoho, 1300 °C results are stacked onto the data in black. The fourth row (bottom) shows values for inclusions from the same samples for which Raman spectroscopy was used to directly measure the density of CO_2 in the vapor bubble (Moore et al., 2015). Note that for both Kīlauea Iki and Kapoho, the Raman-restored CO_2 values include 3 and 4 data points, respectively, that plot offscale at higher values.

quenched and rehomogenized melt inclusions is one of the limitations of the heating experiments, because quenching of the olivine crystals commonly caused them to break into several pieces, leaving smaller inclusions intact for analysis preferentially compared to larger inclusions. We also found that higher Fo olivine survived the heating process better than lower Fo olivine, which also could bias the comparison of heated and naturally quenched inclusions.

Diffusive loss of hydrogen from melt inclusions has been experimentally demonstrated in several previous studies (Hauri, 2002; Massare et al., 2002; Gaetani et al., 2012), and the diffusivity of hydrogen in olivine is strongly temperature dependent (Bucholz et al., 2013). Hauri (2002) showed that experimental heating of Hawaiian melt inclusions in a 1-atm furnace at 1275 °C for less than 10 min in the furnace hot zone did not result in any hydrogen diffusive loss. Use of a high temperature heating stage to redissolve shrinkage bubbles in melt inclusions from a Mauna Loa picrite also showed that hydrogen diffusive loss was minimal (0–10% of initial H_2O of 0.32 wt.%) at temperatures up to 1420 °C if the duration of heating was short (Wallace et al., 2015). In our study, the samples were held at 1400 °C for no more than 15 min. However, because of the nature of the experimental apparatus, they were at high temperature (but outside of the furnace hotspot) during the ~40 min ramp-up time from 800 °C to either 1300 °C or

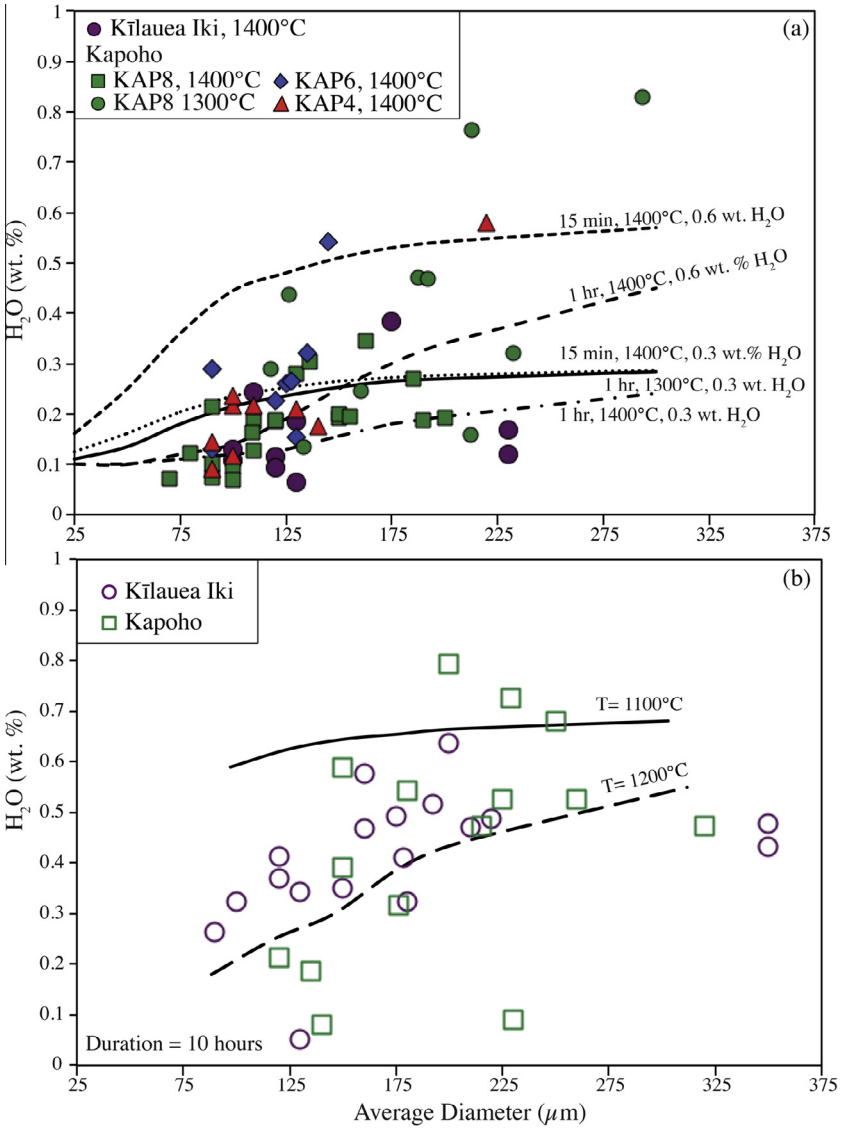

Fig. 6. Melt inclusion average diameter (a proxy for volume) vs. H_2O content. (a) Heated melt inclusions appear to have lost hydrogen by diffusion, with more inclusions plotting between 0.05–0.25 wt.% H_2O compared to naturally quenched inclusions (shown in b). Hydrogen diffusivity is strongly temperature dependent, which explains why the 1400 °C heated melt inclusions experienced greater H diffusive loss than those heated to 1300 °C. Hydrogen diffusive loss at 1400 °C was modeled using Bucholz et al. (2013). Trend lines show several modeled scenarios, with initial H_2O of 0.3 or 0.6 wt.%, durations between 15 min and 1 h, and a comparison to the same conditions at 1300 °C. See text for further discussion. (b) Naturally quenched melt inclusions also show some indication of hydrogen diffusive loss. Smaller melt inclusions appear to have lost more H_2O than larger melt inclusions, due to the higher surface area to volume ratio. The Bucholz et al. (2013) model was also used to simulate scenarios for hydrogen diffusive loss from naturally quenched melt inclusions at 1100 °C and 1200 °C (10 h for both temperatures). For the naturally quenched inclusions, the actual temperature–time history for each inclusion is unknown and is likely quite complex and protracted, and the model curves are intended only as an illustration of how inclusion size affects diffusive loss.

1400 °C. Quenching time in both our experiments and those of Wallace et al. (2015) were very rapid, on the order of a few seconds.

We modeled hydrogen loss from the inclusions using Bucholz et al. (2013). Because the model requires constant temperature, we simulated three sets of conditions to gain insight into the extent of diffusive loss that might have occurred during the experiments: (1) heating time of 15 min at 1400 °C (which does not account for the time the inclusions spent during the ramp up to peak temperature), (2) heating time of one hour at 1400 °C, and (3) heating time of one hour at 1300 °C (to simulate the average conditions the inclusions experienced during ramp up). In all models, initial H_2O was 0.3 or 0.6 wt.%. For heating times of 15 min at 1400 °C, the models do not predict enough hydrogen loss to account for the many very low values (<0.2 wt.%) in the heated inclusions (Fig. 6a). Heating for 1 h at 1400 °C could create the lower H_2O values, but the melt inclusions were not at peak temperature for that long, even when the ramp-up time is considered. Heating at 1300 °C for 1 h is

predicted to have a relatively small effect on H_2O (Fig. 6a), suggesting minimal diffusive loss during the furnace ramp up.

The model results suggest that some of our heated inclusions have lower H_2O than is predicted by diffusive loss according to the Bucholz et al. (2013) model if the inclusions contained 0.3 or 0.6 wt.% before the experiment. This discrepancy could result from our extrapolation of their model to higher temperatures than those at which it is experimentally calibrated (1100–1250 °C). An alternative possibility comes from the observation that the lowest H_2O values in naturally quenched melt inclusions typically occur in the smallest inclusions (Fig. 6b). This suggests that at least some of the low H_2O values in the heated inclusions could reflect low H_2O concentrations in the naturally quenched inclusions before they were heated. The main goals of our study were to determine how much CO_2 is in shrinkage bubbles and then to use that information to calculate accurate pressures of trapping. Because the small amount of dissolved H_2O in Kīlauea melt inclusions contributes little to the total pressure calculation (Fig. 4), the loss of hydrogen by diffusion in our experiments does not significantly affect our interpretations.

5.2. Comparison of heating experiments and Raman data on bubble CO_2 densities

The 1400 °C heating experiments redissolved substantial CO_2 from vapor bubbles back into the melt inclusions. Moore et al. (2015) used Raman spectroscopy to measure the density of CO_2 in shrinkage bubbles in naturally quenched melt inclusions from the same Kīlauea Iki and Kapoho samples as used in this study. They found that Kapoho shrinkage bubbles had similar to higher measured CO_2 densities than Kīlauea Iki. In this section, we compare the results of our heating experiments with estimates of restored CO_2 concentrations based on the Raman data.

The heated Kīlauea Iki melt inclusions have CO_2 concentrations that range from below detection to 588 ppm, with a median of 195 ppm ($n = 10$; Table 1). Moore et al. (2015) used Raman data to estimate the original CO_2 concentration for 32 melt inclusions in six olivine crystals from the same Kīlauea Iki sample. Most of the values are $\leqslant$1000 ppm, and three values are much higher (Fig. 5). Their results show considerable overlap with our heating experiments, but their data extend to higher values and have a much higher median value (570 ppm).

The heated (1400 °C) Kapoho inclusions have CO_2 concentrations of 93–884 ppm, with one value at 1863 ppm, and a median value of 421 ppm ($n = 38$; Fig. 5). Moore et al. (2015) used Raman data to estimate the original CO_2 concentration for 25 melt inclusions in 11 olivine crystals from the Kap8 sample (median 942 ppm CO_2). Most of the values are between 200 and 2000 ppm (Fig. 5), and three values are much higher. As with Kīlauea Iki, their results show considerable overlap with our heating experiments, but their data include even more inclusions with higher values than ours.

At least three factors likely cause the higher CO_2 values for many of the inclusions analyzed by Raman spectroscopy compared to our heating results. First, we analyzed inclusions that had no bubble or only a small bubble after the heating experiment, so our results are biased away from inclusions that might not have homogenized because they had a large bubble. In the Raman dataset (Moore et al., 2015), larger bubble sizes (higher vol.%) correlate with higher restored initial CO_2 concentrations. Second, inclusions that were trapped at higher pressures and therefore had higher CO_2 may not survive the heating process as well because they develop a higher internal pressure during the heating experiment. Third, the bubbles in very small melt inclusions (~5 μm radius) can be analyzed by Raman, whereas the FTIR method required us to focus only on larger melt inclusions, so our dataset is biased towards larger inclusions.

5.3. Quantifying loss of CO_2 to shrinkage bubbles

In this section we compare our experimental results to a post-entrapment crystallization model that provides an independent method for estimating the extent of CO_2 loss to bubbles. Riker (2005) formulated an empirical relationship for Mauna Loa tholeiitic melts between the vol.% bubble formed inside an inclusion as a function of the difference between the trapping and pre-eruption temperatures. The resulting equation is:

$$\text{Bubble vol.\%} = 0.0162\ \Delta T$$

where $\Delta T = T_{trapping} - T_{pre\text{-}eruption}$. For Kīlauea melt inclusions, we estimate trapping and pre-eruption temperatures using the experimentally calibrated thermometer of Helz and Thornber (1987) based on melt MgO content. The pre-eruption MgO used in the thermometer is the uncorrected melt inclusion composition (which represents melt MgO in equilibrium with olivine just before eruption and rapid quenching), whereas the temperature at trapping is calculated using the Petrolog3.1 corrected MgO concentration. For the naturally quenched Kīlauea Iki melt inclusions, estimated trapping temperatures are 1215–1269 °C and pre-eruption temperatures are 1147–1165 °C (see Supplementary Table 1). This method yields ΔT values of 55–115 °C and estimated pre-eruption bubbles of 0.9–1.5 vol.% (Fig. 7). For sample Kap8, trapping temperatures are 1215–1303 °C, similar to Kīlauea Iki, and pre-eruption temperatures are 1145–1229 °C. This yields ΔT values for Kap8 that are more variable than for Kīlauea Iki, ranging from 33–156 °C, yielding bubble volume estimates of 0.5–2.5 vol.%. For sample Kap6, trapping temperatures are 1176–1266 °C and pre-eruption temperatures are 1149–1152 °C. This yields ΔT values ranging from 27 to 115 °C, which overlap with Kīlauea Iki values, yielding pre-eruptive bubble volume estimates of 0.4–1.5 vol.%.

Using these values for pre-eruption bubble vol.%, we estimate how much CO_2 was in the bubbles using Wallace et al. (2015). The results suggest that the amount of the initial bulk CO_2 lost to shrinkage bubbles is in the range of 72–84% for Kīlauea Iki and 55–84% for Kapoho. For both Kīlauea Iki and Kapoho, the calculated CO_2 concentrations overlap with the 1400 °C experimental results and

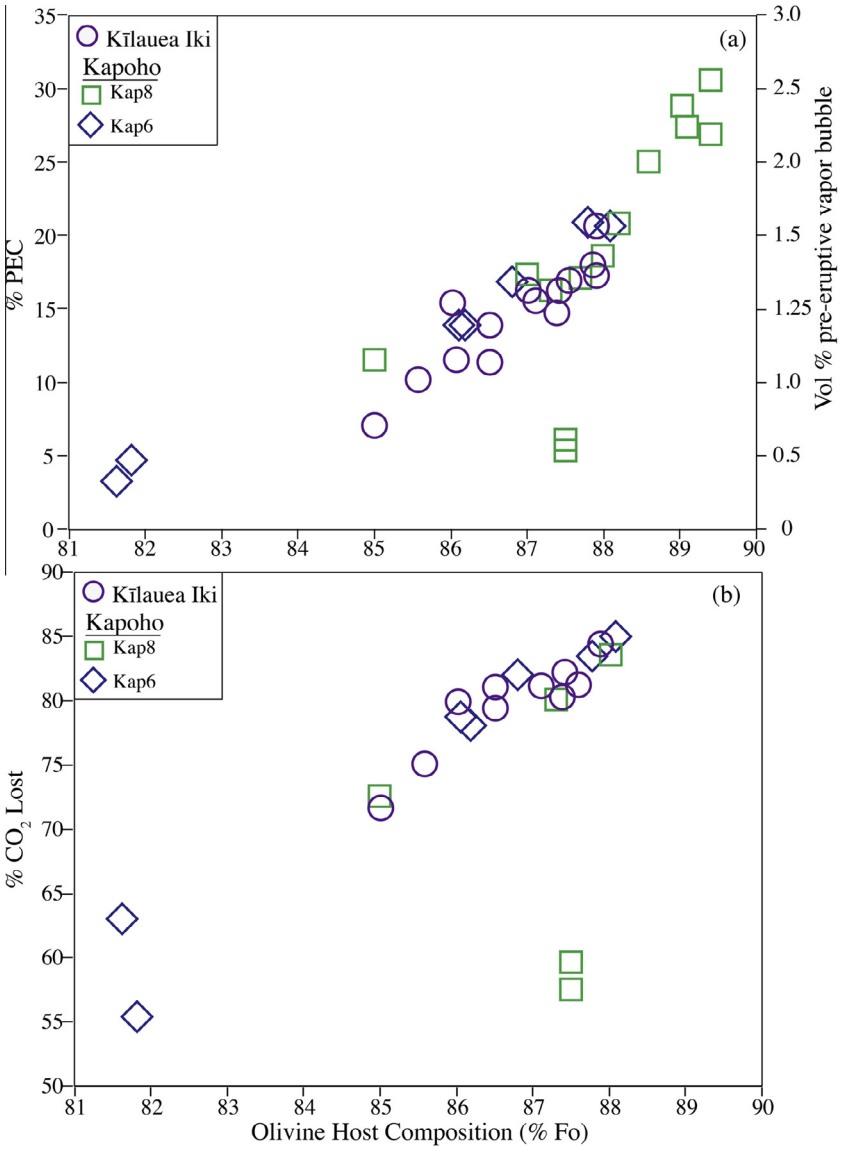

Fig. 7. (a) Olivine host composition vs. the amount of post-entrapment crystallization (PEC) calculated for naturally quenched melt inclusions (left axis) and the vol.% pre-eruptive vapor bubble calculated following the method described in the text (right axis). PEC estimates were calculated using Petrolog3.1. (b) Olivine host composition vs. the calculated % initial CO_2 lost to the pre-eruptive vapor bubble for naturally quenched melt inclusions. A comparison of the relationship between PEC, vapor bubble vol.%, and % initial CO_2 lost from our model to that of Steele-MacInnis et al. (2011), which was used to model melt inclusions at Kīlauea Iki by Sides et al. (2014b), is shown in Supplement Fig. A.3.

extend to higher values that extensively overlap with the higher Raman-restored values (Fig. 5).

Melt inclusions in more Mg-rich olivine typically undergo a larger cooling interval between trapping and eruption than those in lower Mg hosts (Fig. 7). This results in greater PEC for the inclusions in high-Mg olivine, and consequently larger predicted pre-eruption vapor bubbles and greater extents of CO_2 loss to shrinkage bubbles. This helps to explain, in part, why many of the Kapoho melt inclusions have higher restored CO_2 than for Kīlauea Iki. Inclusions from the two suites have similar amounts of dissolved CO_2 in the naturally quenched inclusions (Fig. 5), but the Kapoho samples have olivine crystals that extend to higher Fo contents than those in Kīlauea Iki.

5.4. Olivine crystallization depths

Crystallization pressures of olivine can provide insight into Kīlauea's magma plumbing system. Our data and that of Moore et al. (2015) provide information on vapor saturation pressures at the time of inclusion trapping and can therefore be used to infer crystallization and storage depths. An important consideration in interpreting these pressures is whether the olivine crystals are phenocrysts, are re-entrained from cumulate or earlier-intruded and stored

magma bodies. This question is explored after a general discussion of the crystallization pressures for the various samples.

Vapor saturation pressures were calculated for all inclusions using the VolatileCalc solubility model (Newman and Lowenstern, 2002). There is strong evidence that Kīlauea melts are vapor saturated at crustal pressures (Gerlach and Graeber, 1985; Gerlach, 1986; Gerlach et al., 2002). Therefore the resulting vapor saturation pressures should be equivalent to trapping pressures that can be used to calculate the crystallization depth of the olivine hosts (Anderson and Brown, 1993). We used the depth-density relationship of Ryan (1987) to calculate the crystallization depths from the vapor saturation pressures. This relationship suggests that the bulk density of the crust at shallow levels on the volcano is lower than the density of basalt melt due to the presence of fluid-filled cracks. As the depth increases, the density of the crust increases until it reaches values appropriate for dense, unfractured basalt at around 4.5 km (Ryan, 1987).

The calculated vapor saturation (Table 1) pressures for Kīlauea Iki melt inclusions indicate that most olivine crystallized at $\leqslant$1.5 kbar pressure, which corresponds to depths of $\leqslant$5.5 km (based on the Ryan [1987] depth-density relationship), and more than 50% of the crystallization pressures are in the 1–3 km depth range (Figs. 8 and 9). Even the most primitive olivine from Kīlauea Iki ($Fo_{87–88}$) appear to have crystallized at relatively shallow depths (Fig. 8). One Raman-analyzed inclusion has a much higher CO_2 content indicating a depth as great as 20 km. This is clearly an outlier from the rest of the dataset. The observation that Kīlauea Iki olivines crystallized at depths similar to those inferred for the summit magma chamber (2–5 km) from geophysical data is consistent with the interpretation of Pietruszka et al. (2015) that the more primitive end member magma for the 1959 eruption was likely supplied directly from the summit reservoir.

Heated Kap8 melt inclusions have trapping pressures of ~0.2–3.5 kbar (median 1.0 kbar; Table 1), Kap6 heated melt inclusions have values of ~0.25–0.9 kbar (median 0.5 kbar), and Kap4 heated melt inclusions have values of ~0.25–1.5 kbar (median 1.0 kbar). Unlike Kīlauea Iki olivine, there is a correlation between forsterite content and crystallization depth for Kapoho olivine (Fig. 8), particularly for Kap8, which was erupted with the youngest tephra deposited by Cone Complex/Pu'u Laimana. Inclusion of the Raman dataset (Fig. 9) extends the depth of crystallization for Kap8 olivine, with depths between 3 and 16 km, and one inclusion suggesting a depth as great as 24 km. The combined dataset of heated and Raman-analyzed melt inclusions shows extensive overlap in the crystallization depths of Kīlauea Iki and Kapoho olivines (Fig. 9) However, ~20% of the Kapoho olivines crystallized at greater depths than those from Kīlauea Iki (Fig. 9). Many Kapoho olivine crystals crystallized at depths similar to and greater than those inferred for the deep east rift zone based on geophysical data (3–9 km [~0.8–2.5 kbar]; Poland et al., 2014; Fig. 9).

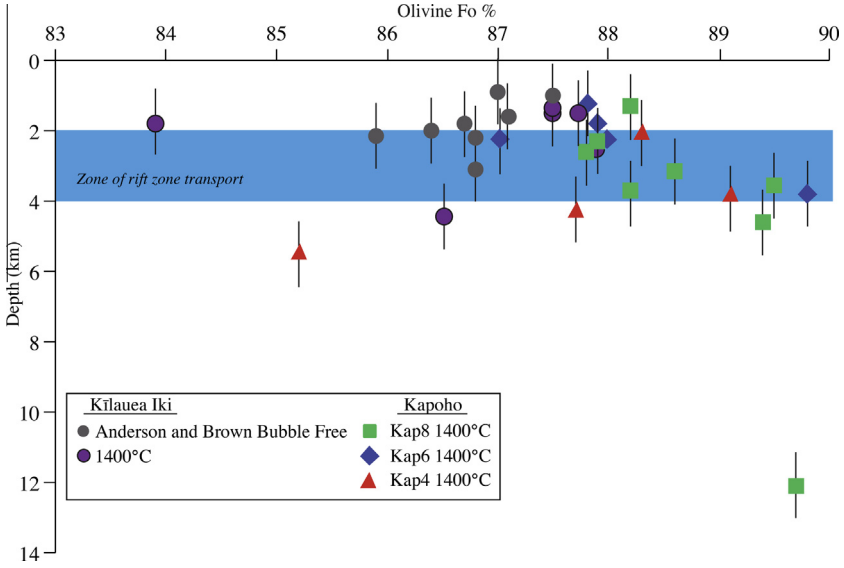

Fig. 8. Olivine host composition vs. estimated crystallization depth for heated (1400 °C) Kīlauea Iki and Kapoho melt inclusions (Kap8, Kap6, and Kap4). The Kīlauea Iki data include bubble-free Iki-22 inclusions from Anderson and Brown (1993). The depths for all melt inclusions were calculated using vapor saturation pressures (Newman and Lowenstern, 2002) and the depth-density relationship of Ryan (1987), in which crustal density increases with depth, approaching the density of unfractured basalt melt as vapor-filled cracks are closed with increasing pressure. For Kīlauea Iki, there does not appear to be any correlation between the forsterite content of the olivine host and the crystallization depth. Kapoho melt inclusions, particularly those from Kap8, suggest that a primitive olivine population (Fo_{89}) crystallized at greater depths than their more differentiated counterparts. The horizontal blue bar represents the depths of rift zone transport suggested by geophysical data (Poland et al., 2014). (For interpretation of the references to colour in this figure legend, the reader is referred to the web version of this article.)

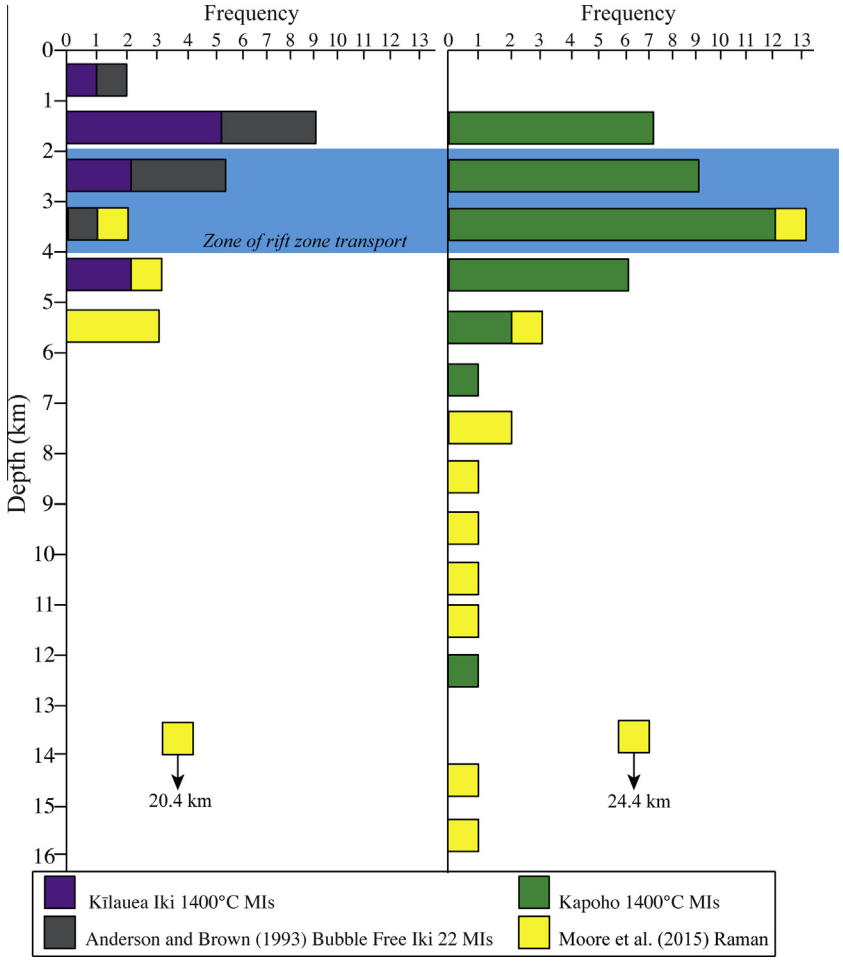

Fig. 9. Histograms of olivine crystallization depths at Kīlauea Iki (left) and Kapoho (right). These histograms include data for experimentally heated melt inclusions from this study, Anderson and Brown's (1993) bubble-free Iki melt inclusions, and results from Raman spectroscopy (Moore et al., 2015). Note that Moore et al. (2015) analyzed multiple inclusions in each olivine crystal. The values shown here for their data are average depths for each crystal based on multiple inclusions, and for this reason, the number of data points from their study on this graph is smaller than are shown on Fig. 5. Depths were calculated as described in Fig. 8. Depth values have ±1 km uncertainty as in Fig. 8. Blue bar shows depth of rift zone transport as in Fig. 8. For each panel, there is one additional Raman-analyzed inclusion with a greater trapping depth than the limit of the axis. (For interpretation of the references to colour in this figure legend, the reader is referred to the web version of this article.)

5.5. Origin of olivine: phenocrysts or re-entrained cumulate

Both Kīlauea Iki and Kapoho erupted olivine-phyric tephra and lava with relatively large olivine crystals (many $\geqslant$2 mm long). The coarse nature of the olivine suggests the crystals might be cumulate in origin and therefore be unrelated to the magma in which they eventually erupted (e.g., Welsch et al., 2013). Kīlauea Iki in particular contains a diversity of olivine types, including normal and reversely zoned crystals (Helz, 1987). Comparison of the compositions of olivine-hosted melt inclusions, bulk rock and matrix glass can clarify the origin of olivine. If melt inclusions have compositions that are similar to matrix glass and bulk rock values, the host crystals may be phenocrysts that either grew and remained entrained in the same magma or were re-entrained cumulate from compositionally similar magmas in the same eruption. For Kīlauea Iki, a plot of CaO vs. Al_2O_3 (Supplementary Fig. A.4a) shows that many of the melt inclusions have CaO/Al_2O_3 ratios similar to bulk rock samples from the first episode of the Kīlauea Iki eruption (Richter et al., 1970; Helz, 1987). While this is permissive of a co-genetic origin for melt inclusions, host olivine crystals, and the host magma, many historical summit lavas at Kīlauea have similar compositions (Garcia et al., 2003), making CaO/Al_2O_3 ratios a poor discriminant. In contrast to the results for Kīlauea Iki, Kapoho melt inclusions have mostly different CaO and Al_2O_3 values than their matrix glass and bulk rock (Supplementary Fig. A.4b), clearly indicating that the Kapoho olivine crystals are antecrysts or xenocrysts.

Incompatible trace elements in the melt inclusions provide a more sensitive tool for investigating the origin of the olivine and examining possible relationships among erupted magma batches. In particular, Garcia et al. (2003)

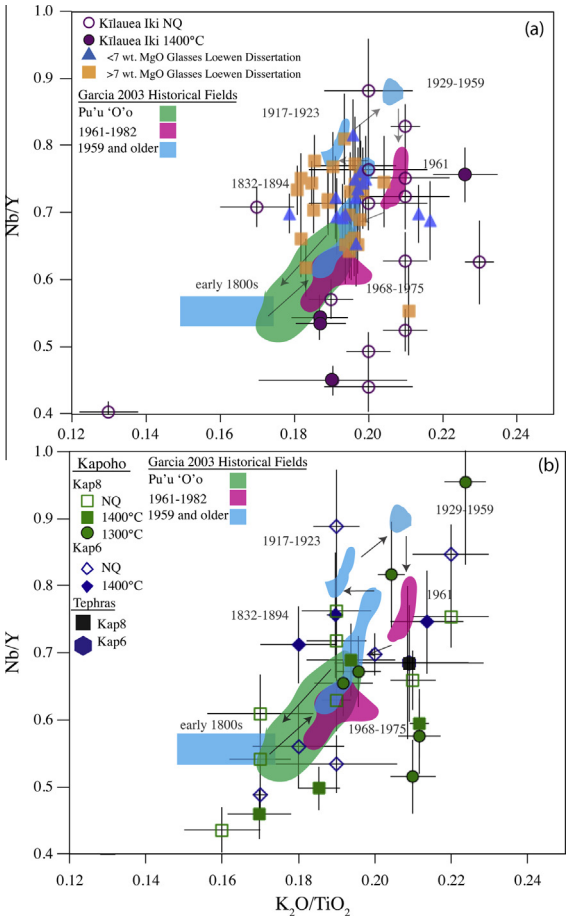

Fig. 10. K_2O/TiO_2 vs. Nb/Y for melt inclusions from Kīlauea Iki (a) and Kapoho (b). Data include both heated and naturally quenched inclusions, as well as tephra glass compositions from Kapoho (Supplementary Table 1) (b). Matrix glass data for Kīlauea Iki are from Loewen (2013). The data are overlaid onto historical fields for K_2O/TiO_2 and Nb/Y in bulk rock samples (Garcia et al., 2003), which show a positive increase in K_2O/TiO_2 and Nb/Y through Kīlauea's historical period until the Kīlauea Iki eruption, after which Nb/Y decreases. Error bars show ±2 standard error uncertainties.

showed that elevated ratios of incompatible elements such as Nb/Y are characteristic of summit lavas erupted at Kīlauea from 1929 to 1959. On a plot of Nb/Y vs. K_2O/TiO_2 (based on Garcia et al., 2003; all elements are incompatible in olivine), the Kīlauea Iki and Kapoho melt inclusions show wide and overlapping ranges of values (Fig. 10). The melt inclusions contain Nb/Y values that span the entire range of 19th and 20th century whole rock values for Kīlauea, and many Kīlauea Iki melt inclusions have lower Nb/Y than matrix glasses (Fig. 10a). This suggests that many olivine crystals in the Kīlauea Iki eruption are likely to be earlier formed crystals (antecrysts) derived from cumulates that were re-entrained by ascending magmas. It is difficult, however, to know what range of Nb/Y values can distinguish phenocrysts from antecrysts because Kīlauea Iki erupted mixed magmas (based on the presence of diverse olivine types; Helz, 1987) that likely formed by mixing of melts with some compositional variability. Such mixing can explain the compositional heterogeneity of both matrix glasses and melt inclusions (Fig. 10a; see also Maclennan et al., 2003) but creates ambiguity in rigorously distinguishing phenocrysts from antecrysts based on melt inclusion data alone. Sides et al. (2014b) also noted a larger variation in incompatible element ratios (e.g., La/Yb) for Kīlauea Iki melt inclusions compared to matrix glasses using a dataset that included many more eruptive episodes. They interpreted the variability in terms of mixing processes and concluded that most olivine crystals were phenocrysts because the melt inclusion values bracket the matrix glasses in composition. For Kapoho melt inclusions, the wide variability in Nb/Y and K_2O/TiO_2 is similar to that for Kīlauea Iki (Figs. 10, A.5), and the Kapoho melt inclusions are mostly distinct from their matrix glasses, consistent with a complex, antecrystic origin for the olivine.

5.6. Implications for Kīlauea's magma plumbing system

The wide range of crystallization depths (~1–16 km) for Kapoho olivine (Fig. 9) and the relatively high CO_2 contents of some of the melt inclusions (Fig. 5) provide insight into magma transport and supply during the eruption. Rift zone eruptions typically involve CO_2-poor magma that outgassed beneath the summit region before shallow lateral transport through the rift system (Gerlach and Graeber, 1985; Gerlach, 1986). Kapoho eruption products have previously been interpreted as the result of magma mixing within the rift zone (Wright and Helz, 1996). Early Kapoho lavas were differentiated, because arriving summit magmas mixed with stored rift zone magma, and lava temperatures increased over a period of 10 days at the Kapoho vent site as hotter magma similar to that erupted at Kīlauea Iki progressively flushed out the stored rift magma. The much wider depth range for Kapoho olivine compared to Kīlauea Iki olivine requires at least some magma transport during the Kapoho eruption from deep beneath the summit region and/or from deep beneath Kīlauea's east rift zone. The shallow and deep portions of the rift zone may be interconnected by a series of almost vertical bladed dikes (Delaney et al., 1990) that allow olivine to settle and accumulate across a large range of depths to form dunitic cumulate bodies (Clague et al., 1995). However, the high CO_2 concentrations in some Kapoho melt inclusions require olivine crystallization from relatively deep melts that had not experienced low pressure degassing at shallow depth beneath the summit or rift zone. Olivine from deeper cumulates in the rift zone could only have been erupted at Kapoho if lateral transport of magma from beneath the summit into the rift occurred at depths as great as 16 km. Alternatively, if the deeply derived olivine crystals came from magma bodies beneath the summit region, they could have been remobilized and then transported laterally through the shallow rift system with the remaining magma from the Kīlauea Iki eruption. Whatever their origin, the deeply derived olivine crystals and their host magma were mixed with stored, more evolved magma in the rift zone, and the mixture was erupted at Kapoho.

6. SUMMARY

We heated olivine from the 1959 Kīlauea Iki and 1960 Kapoho eruptions in a 1-atm furnace to redissolve the CO_2 in shrinkage bubbles, as a means of determining more accurate melt inclusion trapping pressures and olivine crystallization depths. Temperatures (1400 °C) well above the original melt inclusion trapping temperature were necessary to get bubbles to redissolve. The high temperature resulted in some diffusive hydrogen loss, but this does not significantly affect the ability to infer trapping pressure in low-H_2O melt inclusions.

The measured CO_2 concentrations of the experimentally rehomogenized inclusions overlap with values for naturally quenched inclusions from the same samples. However, the heated samples have higher within-sample median CO_2 values compared to naturally quenched inclusions, which we interpret as an indication that at least some of the CO_2 from vapor bubbles redissolved during heating. Modeling of vapor bubble formation and comparison with our data suggest that the naturally quenched melt inclusions lost 55–85% of their initial dissolved CO_2 to shrinkage bubbles that formed after entrapment. Our results for heated inclusions, combined with published Raman measurements of the density of CO_2 in shrinkage bubbles from the same samples we studied (Moore et al., 2015), show that olivine from the early part of the Kīlauea Iki eruption crystallized at <6 km depth, with the majority of olivine in the 1–3 km depth range. This is consistent with the interpretation that the more primitive endmember magma for the 1959 eruption was supplied directly from the summit reservoir (Pietruszka et al., 2015). The Kīlauea Iki melt inclusions have a wide range of Nb/Y ratio that suggests a mix of phenocrysts and xenocrysts. Melt inclusions from Kapoho have a similarly wide range of Nb/Y ratio but have CO_2 contents that require crystallization over a much wider range of depths (~1–16 km). The much wider depth range requires magma transport during the Kapoho eruption from deep beneath the summit region and/or from deep beneath Kīlauea's east rift zone. The deeply derived olivine crystals and their host magma mixed with stored, more evolved magma in the rift zone, and the mixture was later erupted at Kapoho.

ACKNOWLEDGEMENTS

This research was supported by a U.S.G.S. Jack Kleinman Grant and a 2013 Exxon Mobil Geoscience Grant. R.T. would like to thank the staff of the U.S. Geological Survey's Hawaiian Volcano Observatory for their assistance during two weeks of sample collection at Kīlauea. We would also like to thank the National Park Service, the Lyman family, and Sanford Trucking Company for providing access and collection of tephra at the multiple sites on the lower east rift zone. We greatly appreciate the constructive comments of M. Garcia, J. Lowenstern, T. Neal, M. Rowe, and an anonymous reviewer that led to many improvements in the final manuscript. Finally, P.W. would like to express his enormous gratitude to Fred Frey for introducing him to the fascinating world of submarine large igneous provinces, and for teaching him that one should use spider diagrams sparingly, if at all.

APPENDIX A. SUPPLEMENTARY DATA

Supplementary data associated with this article can be found, in the online version, at http://dx.doi.org/10.1016/j.gca.2016.04.020.

REFERENCES

Anderson, Jr., A. T. (1974) Evidence for a picritic, volatile-rich magma beneath Mt. Shasta, California. *J. Petrol.* **15**, 243–267.

Anderson, Jr., A. T. and Brown G. G. (1993) CO_2 contents and formation pressures of some Kīlauean melt inclusions. *Am. Mineral.* **78**, 794–803.

Bucholz C. E., Gaetani G. A., Behn M. D. and Shimizu N. (2013) Post-entrapment modifications of volatiles and oxygen fugacity in olivine-hosted melt inclusions. *Earth Planet. Sci. Lett.* **374**, 145–155.

Bureau H., Pineau F., Metrich N., Semet M. P. and Javoy M. (1998a) A melt and fluid inclusion study of the gas phase at Piton de la Fournaise volcano (Reunion Island). *Chem. Geol.* **147**, 115–130.

Bureau H., Metrich N., Pineau F. and Semet M. P. (1998b) Magma-conduit interaction at Piton de la Fournaise volcano (Reunion Island): a melt and fluid inclusion study. *J. Volcanol. Geotherm. Res.* **84**, 39–60.

Cayol V., Dieterich J. H., Okamura A. T. and Miklius A. (2000) High magma storage rates before the 1983 eruption of Kīlauea, Hawai'i. *Science* **288**, 2343–2346.

Clague D. and Denlinger R. P. (1994) The role of olivine cumulates in destabilizing the flanks of Hawaiian volcanoes. *Bull. Volcanol.* **56**, 425–434.

Clague D., Moore J. G., Dixon J. E. and Friesen W. B. (1995) Petrology of Submarine Lavas from Kīlauea's Puna Ridge, Hawai'i. *J. Petrol.* **36**, 299–349.

Danyushevsky L. V. and Plechov P. (2011) Petrolog 3: integrated software for modeling crystallization processes. *Geochem. Geophys. Geosyst.* **12**, 1–32.

Danyushevsky L. V., Della-Pasqua F. N. and Sokolov S. (2000) Re-equilibration of melt inclusions trapped by magnesian olivine phenocrysts from subduction-related magmas: petrological implications. *Contrib. Mineral. Petrol.* **138**, 68–83.

Danyushevsky L. V., Sokolov S. and Falloon T. J. (2002a) Melt inclusions in olivine phenocrysts: using diffusive re-equilibration to determine the cooling history of a crystal, with implications for the origin of olivine-phyric volcanic rocks. *J. Petrol.* **43**, 1651–1671.

Danyushevsky L. V., McNeill A. W. and Sobolev A. V. (2002b) Experimental and petrological studies of melt inclusions in phenocrysts from mantle-derived magmas: an overview of techniques, advantages, and complications. *Chem. Geol.* **183**, 5–24.

Delaney P. T., Fiske R. S., Miklius A., Okamura A. T. and Sako M. K. (1990) Deep magma body beneath the summit and rift zones of Kīlauea volcano, Hawai'i. *Science* **247**, 1311–1316.

Eaton J. P. and Murata K. J. (1960) How volcanoes grow. *Science* **132**, 925–938.

Edmonds M., Sides I. R., Swanson D. A., Werner C., Martin R. S., Mather T. A., Herd R. A., Jones R. L., Mead M. I., Sawyer G., Roberts T., Sutton A. J. and Elias T. (2013) Magma storage, transport and degassing during the 2008–2010 summit eruption at Kīlauea Volcano, Hawai'i. *Geochim. Cosmochim. Acta* **123**, 284–301.

Edmonds M., Sides I. and Maclennan J. (2015) Insights into mixing, fractionation, and degassing of primitive melts at

Kīlauea volcano, chap. 15. In *Hawaiian Volcanoes, from Source to Surface AGU Monograph*, Vol. 208 (eds. M. Poland, R. Carey, D. Weis and V. Cayol), pp. 323–350. Hawaiian Volcanoes, from Source to Surface AGU Monograph.

Esposito R., Bodnar R. J., Danyushevsky L. V., De Vivo B., Fedele L., Hunter J., Lima A. and Shimizu N. (2011) Volatile evolution of magma associated with the solchiaro eruption in the phlegrean volcanic district (Italy). *J. Petrol.* **52**, 2431–2460.

Gaetani G. A., O'Leary J. A., Shimizu N., Bucholz C. E. and Newville M. (2012) Rapid reequilibration of H_2O and oxygen fugacity in olivine-hosted melt inclusions. *Geology* **40**, 915–918.

Garcia M. O., Pietruzska A. J., Rhodes J. M. and Swanson K. A. (2000) Magmatic processes during the prolonged Pu'u 'Ō'ō eruption of Kīlauea Volcano, Hawai'i. *J. Petrol.* **41**, 967–990.

Garcia M. O., Pietruzska A. J. and Rhodes J. M. (2003) A petrologic perspective of Kīlauea volcano's summit magma reservoir. *J. Petrol.* **44**(12), 2313–2339.

Gerlach T. M. and Graeber E. J. (1985) Volatile budget of Kīlauea volcano. *Nature* **313**, 273–277.

Gerlach T. M. (1986) Exsolution of H_2O, CO_2, and S during eruptive episodes at Kīlauea Volcano, Hawai'i. *J. Geophys. Res.* **91**, 12177–12185.

Gerlach T. M., McGee K. A., Elias T., Sutton A. J. and Doukas M. P. (2002) Carbon dioxide emission rate of Kīlauea Volcano: implications for primary magma and the summit reservoir. *J. Geophys. Res. Solid Earth* **107**(B9), ECV 3-1–ECV 3-15.

Hartley M. E., Maclennan J., Edmonds M. and Thordarson T. (2014) Reconstructing the deep CO_2 degassing behaviour of large basaltic fissure eruptions. *Earth Planet. Sci. Lett.* **393**, 120–131.

Hauri E. (2002) SIMS analysis of volatiles in silicate glasses, 2: isotopes and abundances in Hawaiian melt inclusions. *Chem. Geol.* **183**, 115–141.

Hazlett R. W. (1993) *Geological Field Guide Kīlauea Volcano*. Hawai'i Natural Historay Association.

Helz R. (1987) Diverse olivine types in lava of the 1959 eruption of Kīlauea volcano and their eruption dynamics. *U.S.G.S. Prof. Paper.* **1350**, 691–722.

Helz R. and Thornber C. (1987) Geothermometry of Kīlauea Iki lava lake, Hawai'i. *Bull. Volcanol.* **49**, 651–668.

Johnson M. C., Anderson, Jr., A. T. and Rutherford M. J. (1994) Pre-eruptive volatile contents of magmas. *Rev. Mineral.* **30**, 281–330.

Lloyd A. S., Plank T., Ruprecht P., Hauri E. H. and Rose W. (2013) Volatile loss from melt inclusions in pyroclasts of differing sizes. *Contrib. Mineral. Petrol.* **165**, 129–153.

Loewen M. W. and Kent A. J. (2012) Sources of elemental fractionation and uncertainty during the analysis of semi-volatile metals in silicate glasses using LA-ICP-MS. *J. Anal. At. Spectrom.* **27**, 1502–1508.

Loewen M. W. (2013) *Volatile mobility of trace metals in volcanic systems* Ph.D. dissertation. Oregon State University, Corvallis, p. 217.

Lowenstern J. B. (1995) Applications to silicate melt inclusions to the study of magmatic volatiles. In *Magmas, Fluids and Ore Deposits*, 23 (ed. J. F. H. Thompson). Association of Canada Short Course, Mineralogical, pp. 71–99.

Maclennan J., McKenzie D., Hilton F., Gronvold K. and Shimizu N. (2003) Geochemical variability in a single flow from northern Iceland. *J. Geophys. Res. B: Solid Earth* **108**, doi: 000181501800001.

Massare D., Metrich N. and Clocchiatti R. (2002) High temperature experiments on silicate melt inclusions in olivine at 1 atm: inference on temperatures of homogenization and H_2O concentrations. *Chem. Geol.* **183**, 87–98.

Matzen D. K., Baker M. B., Beckett J. R. and Stolper E. M. (2011) Fe-Mg partitioning between Olivine and high-magnesian melts and the nature of Hawaiian parental liquids. *J. Petrol.* **52**, 1243–1263.

Mironov N., Portnyagin M., Botcharnikov R., Gurenko A., Hoernle K. and Holtz F. (2015) Quantification of the CO_2 budget and H_2O-CO_2 systematics in subduction-zone magmas through the experimental hydration of melt inclusions in olivine at high H_2O pressure. *Earth Planet. Sci. Lett.* **425**, 1–11.

Moore L., Gazel E., Tuohy R., Lloyd A., Esposito R., Steele-MacInnis M., Hauri E. H., Wallace P. J., Plank T. and Bodnar R. J. (2015) Bubbles matter: an assessment of the contribution of vapor bubbles to melt inclusion volatile budgets. *Am. Mineral.* **100**, 806–823.

Murata, K. J., and Richter, D. H., (1966) Chemistry of the lavas of the 1959–60 eruption of Kīlauea Volcano, Hawai'i, in The 1959–60 eruption of Kīlauea volcano, Hawai'i. U.S.G.S. Prof. Paper. 537–A, A1–A26.

Newman S., Stopler E. and Stern R. (2000) H_2O and CO_2 in magmas from the Mariana arc and back arc systems. *Geochem. Geophys. Geosyst.* **1**, 1013.

Newman S. and Lowenstern J. B. (2002) VolatileCalc: a silicate melt-H_2O-CO_2 solution model written in Visual Basic for Excel. *Comput. Geosci.* **28**, 597–604.

Nielsen R. L., Michael P. J. and Sours-Page R. (1998) Chemical and physical indicators of compromised melt inclusions. *Geochim. Cosmochim. Acta* **62**, 831–839.

Pietruszka A. J., Heaton D. E., Marske J. P. and Garcia M. O. (2015) Two magma bodies beneath the summit of Kīlauea Volcano unveiled by isotopically distinct melt deliveries from the mantle. *Earth Planet. Sci. Lett.* **413**, 90–100.

Pietruszka A. J. and Garcia M. O. (1999) The size and shape of Kīlauea Volcano's summit magma storage reservoir: a geochemical probe. *Earth Planet. Sci. Lett.* **167**, 311–320.

Poland M. P., Miklius A., and Montgomery-Brown E. K. (2014) Magma supply, storage, and transport at shield-stage Hawaiian volcanoes. *Characteristics of Hawaiian volcanoes*: *U.S.G.S. Prof. Paper.* **1801**, 179–234.

Qin Z., Lu F. and Anderson A. T. (1992) Diffusive reequilibration of melt and fluid inclusions. *Am. Mineral.* **77**, 565–576.

Rhodes J. M. and Vollinger M. J. (2005) Ferrous/ferric ratios in 1984 Mauna Loa Lavas: a contribution to understanding the oxidation state of hawaiian magmas. *Contrib. Mineral. Petrol.* **149**, 666–674.

Richter D. H., Eaton J. P., Murata K. J., Ault W. U., Krivoy H. L. (1970) Chronological narrative of the 1959–60 Eruption of Kīlauea volcano, Hawai'i. U.S.G.S. Prof. Paper. 537-D,1–73.

Riker J. (2005) *The 1859 Eruption of Mauna Loa Volcano, Hawai'i: controls on the development of long lava channels* Master's thesis. University of Oregon, pp. 117–127.

Roedder E. (1979) Origin and significance of magmatic inclusions. *Bull. Mineral.* **102**, 467–510.

Roggensack K., Hervig R. L., McKnight S. B. and Williams S. N. (1997) Explosive basaltic volcanism from Cerro Negro Volcano: influence of volatiles on eruptive style. *Science* **277**, 1639–1642.

Rowe M. C., Nielsen R. L. and Kent A. J. R. (2006) Anomalously high Fe contents in rehomogenized olivine-hosted melt inclusions from oxidized magmas. *Am. Mineral.* **91**, 82–91.

Rowe M. C., Thornber C. R. and Orr T. (2015) Primitive components, crustal assimilation and magmatic degassing during early 2008 Kīlauea summit eruptive activity. In *Hawaiian Volcanoes: From Source to Surface* (eds. R. Carey, V. Cayol, M. Poland and D. Weis). John Wiley & Sons Inc, Hoboken, NJ, pp. 439–455.

Ryan M. P. (1987) Elasticity and Contractancy of Hawaiian Olivine Tholeiite and its Role in the Stability and Structural Evolution of Subcaldera Magma Reservoirs and Rift Systems. *U.S.G.S. Prof. Paper.* **1350**, 1395–1447.

Ryan M. (1988) The mechanics and three-dimensional internal structure of active magmatic systems, Kīlauea volcano, Hawai'i. *J. Geophys. Res.* **93**, 4213–4248.

Ryan M. P., Koyanagi R. Y. and Fiske R. S. (1981) Modeling the 3-dimensional structure of macroscopic magma transport systems – Applications to Kīlauea Volcano, Hawai'i. *J. Geophys. Res.* **86**, 7111–7129.

Schiavi F., Provost A., Schiano P. and Cluzel N. (2016) P-V-T-X evolution of olivine hosted Melt inclusions during high temperature homogenization treatment. *Geochim. Cosmochim. Acta* **172**, 1–21.

Sides I. R., Edmonds M., Maclennan J., Swanson D. A. and Houghton B. F. (2014a) Eruption style at Kīlauea Volcano in Hawai'i linked to primary melt composition. *Nat. Geosci.* **7**(6), 464–469.

Sides I., Edmonds M., Maclennan J., Houghton B. F., Swanson D. A. and Steele-MacInnis M. J. (2014b) Magma mixing and high fountaining during the 1959 Kīlauea Iki eruption, Hawai'i. *Earth Planet. Sci. Lett.* **40**, 102–112.

Sobolev A. V., Hofmann A. W., Jochum K. P., Kuzmin D. V. and Stoll B. (2011) A young source for the Hawaiian plume. *Nature* **476**, 434–437.

Steele-MacInnis M., Esposito R. and Bodnar R. J. (2011) Thermodynamic model for the effect of post-entrapment crystallization on the H_2O-CO_2 systematics of vapor-saturated, silicate melt inclusions. *J. Petrol.* **52**, 2461–2482.

Thornber C. R., Heliker C. C., Sherrod D. R., Kauahikaua J. P., Mikilius A., Okubo P. G., Trudell F. A., Budahn J. R., Ridley W. I. and Meeker G. P. (2003) Kīlauea east rift zone magmatism: an episode 54 perspective. *J. Petrol.* **44**, 1525–1559.

Thornber C. R., Orr T. R., Heliker C. and Hoblitt R. P. (2015) Petrologic testament to changes in shallow magma storage and transport during 30+ years of recharge and eruption at Kīlauea Volcano, Hawai'i. In *Hawaiian Volcanoes: From Source to Surface* (eds. R. Carey, V. Cayol, M. Poland and D. Weis). John Wiley & Sons Inc, Hoboken, NJ, pp. 147–188.

Tilling R. I. and Dvorak J. J. (1993) Anatomy of a basaltic volcano. *Nature* **363**, 125–132.

Vigouroux N., William-Jones A. E., Wallace P. J. and Staudacher T. (2009) The November 2002 eruption of Piton de la Fournaise, Reunion: tracking the thermal evolution of magma using melt inclusions. *Bull. Volcanol.* **71**, 1077–1089.

Vinet N. and Higgins M. D. (2010) Magma solidification processes beneath Kīlauea Volcano, Hawai'i: a quantitative textural and geochemical study of the 1969–1974 Mauna Ulu lavas. *J. Petrol.* **51**, 1297–1332.

Wallace P. J. and Anderson A. T. (1998) Effects of eruption and lava drainback on the H_2O contents of basaltic magmas at Kīlauea Volcano. *Bull. Volcanol.* **59**, 327–344.

Wallace P. J., Kamenetsky V. S. and Cervantes P. (2015) Melt Inclusion CO_2 contents, pressures of olivine crystallization and the problem of shrinkage bubbles. *Am. Mineral.* **100**(4), 787–794.

Welsch B., Faure F., Famin V., Baronnet A. and Bachelery P. (2013) Dendritic crystallization: a single process for all the textures of olivine in basalts. *J. Petrol.* **54**, 539–574.

Wright T. L. (1973) Magma mixing as illustrated by the 1959 eruption of Kīlauea Volcano, Hawai'i. *Geol. Soc. Am. Bull.* **84**, 849–858.

Wright T. L. and Fiske R. (1971) Origin of the differentiated and hybrid lavas of Kīlauea volcano, Hawai'i. *J. Petrol.* **12**, 1–65.

Wright T. L. and Helz R. (1996) Differentiation and magma mixing on Kīlauea's east rift zone: a further look at the eruptions of 1955 and 1960. Part. II. The 1960 lavas. *Bull. Volcanol.* **57**, 602–630.

Wright T. L. and Klein F. W. (2006) Deep magma transport at Kīlauea Volcano. *Lithos* **87**, 50–79.

Wright T. L. and Klein F. W. (2014) Two hundred years of magma transport and storage at Kīlauea Volcano, Hawai'i, 1790–2008: U.S.G.S. Prof. Paper. 1806, p. 240.

Associate editor: Michael Garcia